

# Comprehensive Electric Arc Furnace Model for Simulation Purposes and Model-Based Control

Amirhossein Fathi, Yadollah Saboohi,\* Igor Škrjanc, and Vito Logar

The paper presents a comprehensive electric arc furnace (EAF) model, developed for simulation and model-based control of the EAF processes. The model consists of three sub models, i.e., (i) arc model; (ii) chemical and slag model; and (iii) heat-transfer model. Arc model predicts the amount of energy dissipated from the arcs using arc currents and arc lengths; chemical and slag model calculates chemical energy and changes of elements/compounds, slag height and slag quality; while the heat-transfer model uses calculations of the other two models in order to establish a reference energy system (RES) for each zone in the EAF due to the variations in arc length, slag height, and bath height. The overall EAF model is based on fundamental thermodynamic and heat-transfer laws, reaction kinetics, and experimental equations. Governing equations describing the processes inside the EAF are of the first order. The validation of the model has shown that the model provides accurate estimation of the EAF process values, such as bath temperature as well as steel and slag compositions. The estimations made by the model are comparable to the measured EAF data, which allows the model to be used for comprehensive analysis of the EAF operation, process monitoring, establishing energy, and mass balance or model-based control of several process variables.

## 1. Introduction

EAFs are widely used to smelt and refine direct reduced iron (DRI) and steel scrap. The share of the steel produced in electric furnaces in the year 2011 was almost 30%<sup>[1]</sup> of the total steel produced in the world. Considering the difference between the minimum theoretical (360 kWh ton<sup>-1</sup>)<sup>[2]</sup> and the actual energy consumption (580–670 kWh ton<sup>-1</sup>)<sup>[2]</sup> of a typical EAF, a significant reduction potential of the energy consumption can be observed. To

reduce the energy consumption of a modern EAF, possessing an accurate EAF model in a combination with a model-based control can be of crucial importance. In order to fulfill the requirements of a model-based control algorithm, the underlying models must implement all of the crucial EAF processes, state variables, and independent variables.

Thus far, several EAF models have been developed in order to simulate the EAF processes in different extent. Considering the results of different studies, empirical mathematical models have the edge when trying to achieve the aforementioned goals over other theoretical models. One of the first EAF models was developed by Bekker et al.,<sup>[3]</sup> which is able to predict the EAF phenomena with 14 state variables and first order linear differential equations based on laws of thermodynamic and empirical equations. Considering the lack of model validation, influence of slag height, and arc length on reference energy system, the model is oversimplified and results of the model can hardly represent a practical implementation of an EAF. However, many EAF models have been developed based on the concept proposed by Bekker et al.<sup>[3]</sup> MacRosty and Swartz<sup>[4]</sup> have considered an EAF with four zones (gas, slag–metal interaction, molten steel, and solid scrap); however, due to

---

[\*] Prof. Y. Saboohi  
Sharif Energy Research Institute (SERI), Sharif University of  
Technology, Azadi Ave., Tehran, Iran  
Email: saboohi@sharif.ir  
A. Fathi  
Department of Energy Engineering, Sharif University of Technology,  
Azadi Ave., Tehran, Iran  
Prof. I. Škrjanc, V. Logar  
Laboratory of Modelling, Simulation and Control, Faculty of Electrical  
Engineering, University of Ljubljana, Tržaška 25, SI-1000, Ljubljana,  
Slovenia

simplification of the model some heat transfers inside the EAF are omitted. Logar et al.<sup>[5,6]</sup> have proposed an EAF model, considering a combination of two modules (heat-/mass-transfer and thermo-chemical), where the thermo-chemical model describes the chemical reactions, rates of elements/compounds change, chemical energy, and slag height, while the heat/mass transfer model uses the data of the thermo-chemical module and computes the rate of mass/temperature change in different EAF zones. In this model, the EAF is divided into seven zones with similar physical and chemical properties, which increases the accuracy and eases the calculation of the heat transfer. Similarly to other EAF models, the model considers the arc energy dissipation mechanisms to be constant, meaning that variations in arc length, slag height, slag properties, and batch height are not considered when calculating the energy transferred to each zone. All of these are important due to the calculation accuracy, especially when estimating temperature and composition of the steel.

The model presented here is a continuation of the work proposed by Logar et al.,<sup>[5,6]</sup> however, a significant part of the model has been modified or replaced in order to achieve a better match between the estimated and the measured EAF data. The most significant changes in the presented model are the following: additional arc model is used to estimate the arc energy dissipation, modified chemical model is used to increase the speed of calculation as well as estimation accuracy for reactions, chemical energy and slag quality, modified heat-radiation model is used to reduce the time complexity and increase calculation accuracy, and finally redesigned and remodeled thermal model is used to calculate the effect of arc length, slag and bath height on the energies transferred to each of the EAF zones. Moreover, the enhanced model is more precise at simulating discontinuous feeds in the EAF. Eventually, the presented model provides a possibility of slag height and arc length being adjusted through manipulated variables, which are a subject to model and operation constraints, such as slag quality, production costs, etc.; meaning that the model can be used to optimize energy and material consumption [through simultaneous adjustment of the arc lengths (via electrode movement), arc currents (via transformer tap) and slag height (by injecting carbonaceous materials, oxygen, and slag formers)], while maintaining desired steel quality.

The notations used in this paper are similar to our previous works,<sup>[5,6]</sup> with the variables that are widely used:  $Q_x$  represents the change of energy in zone  $x$ ;  $T_x$ ,  $L_x$ ,  $r_x$  represent the temperature, length and radius of zone  $x$ ,  $m_x$  indicates the mass of an element, compound or zone  $x$ ,  $M_x$  is the molar mass of an element or compound  $x$ ,  $Q_{\text{mech},x-y}$  represents the energy transferred from zone  $x$  to zone  $y$  through mechanism mech (if there is more than one mechanism of energy transfer between the zones, otherwise it is shown with  $Q_{x-y}$ ).

## 2. The Framework of the Model

The model framework as shown by Figure 1 has been developed according to the actual EAF process and includes three modules, i.e., (i) arc module; (ii) chemical and slag module; and (iii) heat-transfer module. The arc module calculates the dissipation of the arc energy, arc shape, and arc voltage by using the arc length and arc current. The chemical and slag module calculates the rates of change of compounds and elements, chemical energy of each reaction, slag quality, slag, basicity, slag height, and relative pressure, using the independent variables such as off gas fan power, slip-gap size, carbon injection rate, and oxygen lancing rate. The heat-transfer module estimates the temperatures of all EAF zones and mass transfers by using the arc energy dissipation from the arc module, chemical energy from the chemical, and slag module and hot heel amount (as the external variable). Figure 1 presented in the first part of our work<sup>[7]</sup> shows the conceptual representation of the EAF model to predict main phenomena represented in Figure 1.

### 2.1. Assumptions and Simplification

In order to adequately describe the complex phenomena in the EAF, the model is based on the following assumptions and simplifications.

Arc module:

1. Electric arc follows the ideal gas law.

Chemical and slag module:

1. gas pressure in the EAF free board follows the ideal gas law,
2. all oxides are transferred to the slag layer,
3. reaction between the electrodes and the oxygen results in a complete combustion,
4. gas temperature in the slag zone is assumed to be equal to liquid slag zone,
5. superficial gas velocity is calculated with slag forming and injected gases in the slag layer,
6. elements in steel bath and solid scrap are distributed uniformly.

Heat-transfer module:

1. solid scrap (solid slag) is surrounded by liquid scrap (liquid slag),
2. gas burners are engaged before the formation of the slag, since their efficiency decreases significantly with increasing temperature. Therefore, the energy released is transferred to lSc, sSc, and gas zones,
3. all three electrodes are considered as one electrode having an equivalent effective lateral (electrode height

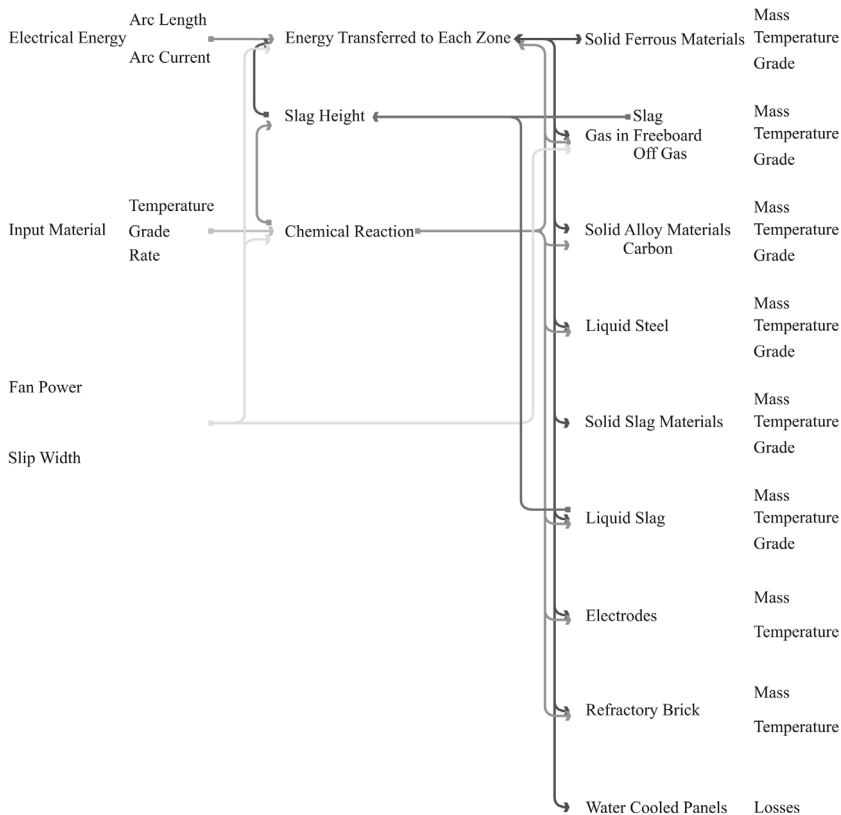


**Figure 1.** Model framework according to the actual EAF process.

inside the EAF) and bottom area. When computing ohmic losses, three electrodes are considered,

4. temperature of the water-cooled panels is constant (this is usually true and is achieved using a separate controller for cooling-water flow),
5. electric arc is considered as a black body when emitting radiative energy and as a transparent body when receiving radiative energy.<sup>[4,5]</sup>

## 2.2. Arc Module

The arc module, which describes the behavior of the electric arcs and dissipation of the arc energy is based on the channel arc model (CAM) and is described in greater detail in Fathi et al.<sup>[7]</sup> The module uses two independent variables (arc length and arc current) as inputs and five output variables (arc energy dissipation mechanisms: radiation, convection and conduction, arc voltage, and arc radius).

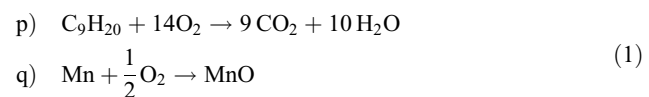
## 2.3. Chemical and Slag Module

The chemical and slag module describes the behavior of the chemical reactions, i.e., oxidation/reduction of elements and compounds and other mechanisms influenced

by them, i.e., chemical energies, slag properties, slag height, and relative pressure. **Figure 2** shows the relations between the influential variables in the module together with other parts of the model, i.e., arc module and heat transfer module.

### 2.3.1. Rates of Change due to Reactions and Injection

This part of the chemical model is similar to the previous work done,<sup>[6]</sup> however, some equations have been revised or added in order to achieve a better match between measured and simulated results (steel and slag composition). The modifications made have been divided into two groups of equations, i.e., (i) revised equations; and (ii) revised calculation of the lanced oxygen fractions for element oxidation. In this model, in addition to existing 15 reactions Equation 1,<sup>[6]</sup> one reaction is added and one reaction them is modified as shown in Equation 1.



**2.3.1.1. Revised Chemical Equations:** The rates of change of elements and compounds are dependent on reactions, injection, and fusion; whereas, this section only focuses on the rates as a consequence of reactions and

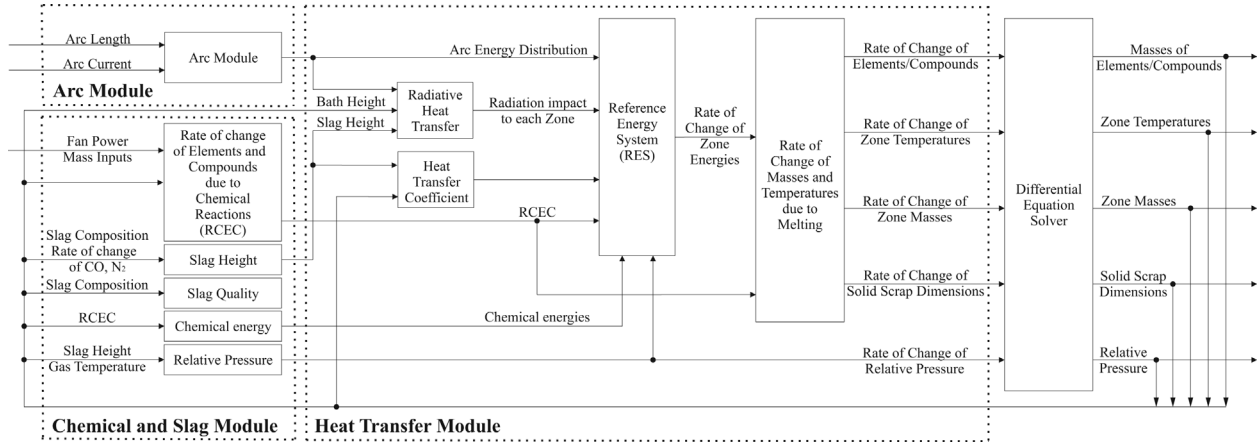


Figure 2. Relations between different parts of the EAF module.

injection. The modified and/or added mechanisms in comparison to our previous work are represented by Equation 2–12, where each equation represents a rate of change of a particular element/compound, with similar notation to our previous work.<sup>[6]</sup> Graphite injection as a carbonaceous material is added to the calculations. It is assumed that graphite and FeO react immediately after injection<sup>[8]</sup> according to reaction described in Equation 1.<sup>[6]</sup> Graphite injection has effect on the rate of change of FeO ( $x7_{d9}$ ), Fe ( $x8_{d9}$ ), CO ( $x9_{d2}$ ), and N<sub>2</sub> ( $x11_{d4}$ ). For every 150 kg of injected graphite, approximately 1 kg of nitrogen is injected as carrier gas.<sup>[3]</sup>

$$\begin{aligned} x1_{d3} &= -P_{O_2-C_{inj}}CO C_{inj} \\ x1_{d4} &= -P_{O_2-C_{inj}-CO_2}C_{inj} \\ x1_{d5} &= -2\frac{M_C}{M_{O_2}}O2_{lance}K_{O_2-C_L-CO} \end{aligned} \quad (2)$$

$$\begin{aligned} x1_{d6} &= -\frac{M_C}{M_{O_2}}O2_{lance}K_{O_2-C_L-CO_2} \\ x2_{d2} &= -2\frac{M_C}{M_{O_2}}O2_{lance}K_{O_2-C_D-CO}, \\ x2_{d5} &= -\frac{M_C}{M_{O_2}}O2_{lance}K_{O_2-C_D-CO_2}, \end{aligned} \quad (3)$$

$$\begin{aligned} x2_{d6} &= \left[ 90\left(\frac{D_{tip}}{250}\right)^2 \left(1 - \frac{V_{arc}}{120}\right) \right] \text{ for } V_{arc} < 120, \\ x3_{d2} &= -\frac{M_{Si}}{M_{O_2}}O2_{lance}K_{O_2-SiO_2}, \end{aligned} \quad (4)$$

$$\begin{aligned} x4_{d3} &= -2\frac{M_{Mn}}{M_{Si}}x3_{d3}, \\ x4_{d4} &= -2\frac{M_{Mn}}{M_{O_2}}O2_{lance}K_{O_2-MnO}, \end{aligned} \quad (5)$$

$$\begin{aligned} x5_{d1} &= -kd_{Cr-1}(X_{Cr} - X_{Cr}^{eq}), \\ x5_{d2} &= -\frac{4}{3}\frac{M_{Cr}}{M_{O_2}}O2_{lance}K_{O_2-Cr_2O_3}, \end{aligned} \quad (6)$$

$$x6_{d1} = -kd_P(X_P - X_P^{eq}), \quad (7)$$

$$x7_{d9} = -Gr_{inj}\frac{M_{FeO}}{M_C}, \quad (8)$$

$$x8_{d9} = -\frac{M_{Fe}}{M_C}x7_{d9}, \quad (9)$$

$$x9_{d2} = -\frac{M_{CO}}{M_C}(x1_{d3} + x1_{d5} + x2_{d1} + x2_{d2} + x2_{d4} - Gr_{inj}), \quad (10)$$

$$\begin{aligned} x10_{d2} &= -2M_{CO_2}K_{AIR_1}k_{PR}r_P, \\ x10_{d7} &= -\frac{M_{CO_2}}{M_C}(x1_{d4} + x1_{d6} + x2_{d5}) \end{aligned} \quad (11)$$

$$x11_{d4} = \frac{1}{x}Gr_{inj}, \quad (12)$$

where  $P_{O_2-C_{inj}-i}$  is the share of carbon that results in incomplete (if  $i$  substituted with CO) and complete (if  $i$  substituted with CO<sub>2</sub>) combustion,  $K_{O_2-C_L-i}$  and  $K_{O_2-C_D-i}$  are the fractions of the lanced oxygen consumed for oxidizing carbon injected and carbon dissolved to  $i$  (CO and CO<sub>2</sub>), respectively,  $x2_{d6}$  represents the rate of electrode tip dissolution,<sup>[9]</sup>  $D_{tip}$  represents the electrode diameter [mm] and  $V_{arc}$  the arc voltage [V].

2.3.1.2. Rate of Graphite Electrode Change: Dissolution and oxidation are two mechanisms considered for estimation of the electrode consumption in the model:

rate of electrode tip dissolution ( $-x_{2,d6}$ ) as presented in Equation 3 and average oxidation rate of electrode tip and side expressed with Equation 36 in our previous work.<sup>[6]</sup> In compare to the previous work,<sup>[6]</sup> the average oxidation rate of electrode tip ( $\text{kg (kA h)}^{-1}$ ) are found according to the charge:  $R_{\text{tip}} = [0.013 - (\frac{DH}{100})0.007]^{[9]}$  for EAF charging continuously DRI/HBI ( $DH$  is the % of DRI/HBI continuously charged into the EAF) or  $R_{\text{tip}} = [0.0913H - 0.0808]^{[9]}$  for scrap based EAF ( $H$  depends on operation conditions).

**2.3.1.3. Revised Calculation of the Lanced Oxygen Fractions:** The share of each component to react with the lanced oxygen is considered as a function of the component passion to react with oxygen and oxygen lancing presence as described by Equations 13–24.

$$\gamma_{\text{O}_2-\text{FeO}} = \mu \frac{m_{\text{Fe}}}{\sum_i m_i} i = \text{Fe, C, Cr, Si and Mn} \quad (13)$$

$$\beta_{\text{FeO}-\text{O}_2-\text{C}_{\text{inj}}} = P_{\text{FeO}-\text{O}_2-\text{C}_{\text{inj}}} \left( \frac{C_{\text{inj}}}{C_{\text{inj}} + 10^{-12}} \right), \quad (14)$$

$$P_{\text{O}_2-\text{C}_{\text{inj}}-\text{CO}} = 2 \frac{M_{\text{C}}}{M_{\text{O}_2}} \frac{\psi_{\text{O}_2-\text{C}_{\text{inj}}-\text{CO}} \beta_{\text{FeO}-\text{O}_2-\text{C}_{\text{inj}}}}{C_{\text{inj}} + 10^{-12}}, \quad (15)$$

$$P_{\text{O}_2-\text{C}_{\text{inj}}-\text{CO}_2} = \frac{M_{\text{C}}}{M_{\text{O}_2}} \frac{(1 - \psi_{\text{O}_2-\text{C}_{\text{inj}}-\text{CO}}) \beta_{\text{FeO}-\text{O}_2-\text{C}_{\text{inj}}}}{C_{\text{inj}} + 10^{-12}}, \quad (16)$$

$$K_{\text{O}_2-\text{FeO}} = \gamma_{\text{O}_2-\text{FeO}} - \beta_{\text{FeO}-\text{O}_2-\text{C}_{\text{inj}}}, \quad (17)$$

$$K_{\text{O}_2-\text{Cr}_2\text{O}_3} = (1 - \gamma_{\text{O}_2-\text{FeO}}) \frac{\alpha_{\text{Cr}} m_{\text{Cr}}}{\alpha_{\text{C-L}} m_{\text{C-L}} + \alpha_{\text{C-D}} m_{\text{C-D}} + \alpha_{\text{Cr}} m_{\text{Cr}} + \alpha_{\text{Si}} m_{\text{Si}} + \alpha_{\text{Mn}} m_{\text{Mn}}}, \quad (18)$$

$$K_{\text{O}_2-\text{SiO}_2} = (1 - \gamma_{\text{O}_2-\text{FeO}}) \frac{\alpha_{\text{Si}} m_{\text{Si}}}{\alpha_{\text{C-L}} m_{\text{C-L}} + \alpha_{\text{C-D}} m_{\text{C-D}} + \alpha_{\text{Cr}} m_{\text{Cr}} + \alpha_{\text{Si}} m_{\text{Si}} + \alpha_{\text{Mn}} m_{\text{Mn}}}, \quad (19)$$

$$K_{\text{O}_2-\text{MnO}} = (1 - \gamma_{\text{O}_2-\text{FeO}}) \frac{\alpha_{\text{Mn}} m_{\text{Mn}}}{\alpha_{\text{C-L}} m_{\text{C-L}} + \alpha_{\text{C-D}} m_{\text{C-D}} + \alpha_{\text{Cr}} m_{\text{Cr}} + \alpha_{\text{Si}} m_{\text{Si}} + \alpha_{\text{Mn}} m_{\text{Mn}}}, \quad (20)$$

$$K_{\text{O}_2-\text{C}_L-\text{CO}} = (1 - \gamma_{\text{O}_2-\text{FeO}}) \frac{\zeta_{\text{L-CO}} \alpha_{\text{C-L}} m_{\text{C-L}}}{\alpha_{\text{C-L}} m_{\text{C-L}} + \alpha_{\text{C-D}} m_{\text{C-D}} + \alpha_{\text{Cr}} m_{\text{Cr}} + \alpha_{\text{Si}} m_{\text{Si}} + \alpha_{\text{Mn}} m_{\text{Mn}}}, \quad (21)$$

$$K_{\text{O}_2-\text{C}_L-\text{CO}_2} = (1 - \gamma_{\text{O}_2-\text{FeO}}) \frac{(1 - \zeta_{\text{L-CO}}) \alpha_{\text{C-L}} m_{\text{C-L}}}{\alpha_{\text{C-L}} m_{\text{C-L}} + \alpha_{\text{C-D}} m_{\text{C-D}} + \alpha_{\text{Cr}} m_{\text{Cr}} + \alpha_{\text{Si}} m_{\text{Si}} + \alpha_{\text{Mn}} m_{\text{Mn}}}, \quad (22)$$

$$K_{\text{O}_2-\text{C}_D-\text{CO}} = (1 - \gamma_{\text{O}_2-\text{FeO}}) \frac{\zeta_{\text{D-CO}} \alpha_{\text{C-D}} m_{\text{C-D}}}{\alpha_{\text{C-L}} m_{\text{C-L}} + \alpha_{\text{C-D}} m_{\text{C-D}} + \alpha_{\text{Cr}} m_{\text{Cr}} + \alpha_{\text{Si}} m_{\text{Si}} + \alpha_{\text{Mn}} m_{\text{Mn}}}, \quad (23)$$

$$K_{\text{O}_2-\text{C}_D-\text{CO}_2} = (1 - \gamma_{\text{O}_2-\text{FeO}}) \frac{(1 - \zeta_{\text{D-CO}}) \alpha_{\text{C-D}} m_{\text{C-D}}}{\alpha_{\text{C-L}} m_{\text{C-L}} + \alpha_{\text{C-D}} m_{\text{C-D}} + \alpha_{\text{Cr}} m_{\text{Cr}} + \alpha_{\text{Si}} m_{\text{Si}} + \alpha_{\text{Mn}} m_{\text{Mn}}}, \quad (24)$$

where  $\gamma_{\text{O}_2-\text{FeO}}$  is the fraction of  $\text{O}_2$  used to oxidize Fe in the case of non-simultaneous lancing of  $\text{O}_2$  and C (it describes the potential of Fe to react with  $\text{O}_2$  [ $\mu$ ] and the probability of Fe presence in the  $\text{O}_2$  lancing zone),  $\alpha_i$  denotes the passion of element  $i$  to react with  $\text{O}_2$ ,  $C_{\text{inj}}$  is carbon injection rate,  $m_i$  is the mass of dissolved element  $i$  (in molten form). When carbon is injected into the steel bath, the probability of Fe oxidation reduces [ $P_{\text{FeO}-\text{O}_2-\text{C}_{\text{inj}}}$ ], which is represented by  $\beta P_{\text{FeO}-\text{O}_2-\text{C}_{\text{inj}}}$ . When C injection and  $\text{O}_2$  lancing are engaged simultaneously, the probability of  $\text{CO}_2$  formation in injecting moment is shown by  $\psi_{\text{O}_2-\text{C}_{\text{inj}}-\text{CO}_2}$  and for CO formation, it is represented by  $\psi_{\text{O}_2-\text{C}_{\text{inj}}-\text{CO}}$  in Equation 15 and 16. Finally,  $\zeta_{i-j}$  is to represent the fraction of lanced oxygen consumed for oxidizing  $i$  (carbon injected and carbon dissolved) to  $j$  ( $\text{CO}$  and  $\text{CO}_2$ ).

### 2.3.2. Relative Pressure

The relative pressure in an EAF free board is dependent on gases exiting the chemical reactions and off-gas fan speed. If the relative pressure is negative, air will leak into EAF, otherwise the gases will exit the EAF through the hatches. The relative pressure can be obtained following the ideal gas law; meaning that it is a function of change of temperature, volume and masses as described by Equation 25:

$$r_p = \frac{n_{\text{gas}} R_{\text{gas}} T_{\text{gas}}}{V_{\text{gas}}} \left[ \frac{\dot{n}_{\text{gas}}}{n_{\text{gas}}} + \frac{\dot{T}_{\text{gas}}}{T_{\text{gas}}} - \frac{\dot{V}_{\text{gas}}}{V_{\text{gas}}} \right] \quad (25)$$

where  $V_{\text{gas}}$ ,  $n_{\text{gas}}$ , and  $\dot{n}_{\text{gas}}$  are obtained by Equations 26–28, respectively:

$$V_{\text{gas}} = V_{\text{EAF}} - V_{\text{ISc}} - V_{\text{sSc}} - V_{\text{sSI}} - V_{\text{ISI}} - V_{\text{electrodes}}, \quad (26)$$

$$n_{\text{gas}} = \frac{m_{\text{CO}}}{M_{\text{CO}}} + \frac{m_{\text{CO}_2}}{M_{\text{CO}_2}} + \frac{m_{\text{O}_2}}{M_{\text{O}_2}} + \frac{m_{\text{N}_2}}{M_{\text{N}_2}} + \frac{m_{\text{CH}_4}}{M_{\text{CH}_4}} + \frac{m_{\text{H}_2\text{O}}}{M_{\text{H}_2\text{O}}}, \quad (27)$$

$$\dot{n}_{\text{gas}} = \frac{\dot{m}_{\text{CO}}}{M_{\text{CO}}} + \frac{\dot{m}_{\text{CO}_2}}{M_{\text{CO}_2}} + \frac{\dot{m}_{\text{O}_2}}{M_{\text{O}_2}} + \frac{\dot{m}_{\text{N}_2}}{M_{\text{N}_2}} + \frac{\dot{m}_{\text{CH}_4}}{M_{\text{CH}_4}} + \frac{\dot{m}_{\text{H}_2\text{O}}}{M_{\text{H}_2\text{O}}} \quad (28)$$

where  $V_i$  is the volume of the corresponding EAF zone (complete EAF, liquid scrap, etc.) and  $m_{\text{CH}_4}$  represents the share of the natural gas that has not reacted in the combustion reaction.

### 2.3.3. Energy of Chemical Reactions

Chemical energy has been calculated by the reaction enthalpy similar to our previous work.<sup>[6]</sup> Some coefficients are changed due to stoichiometric observation, with some additional reactions in comparison to the previous model. Equations 29–39 describe the change of enthalpy of those reactions, where suffixes “a”–“q” denote the associated reactions from Equation 1:<sup>[6]</sup>

$$\Delta H_{T-b} = \frac{x_{2d2} - \text{Gr}_{\text{Inj}}}{M_C} \left[ \Delta H_{\text{CO}} - \Delta H_{\text{C-S}} - \Delta H_{\text{FeO}} + \int_{298}^{T_{\text{isc}}} C_{\text{P,Fe}} + C_{\text{P,CO}} - C_{\text{P,C}} - C_{\text{P,FeO}} dT \right], \quad (29)$$

$$\Delta H_{T-d} = \frac{x_{3d1}}{M_{\text{Si}}} \left[ \Delta H_{\text{SiO}_2} + \Delta H_{\text{SiO}_2-s} - 2\Delta H_{\text{FeO}} - \Delta H_{\text{Si-S}} + \int_{298}^{T_{\text{isc}}} 2C_{\text{P,Fe}} + C_{\text{P,SiO}_2} - 2C_{\text{P,FeO}} - C_{\text{P,Si}} dT \right], \quad (30)$$

$$\Delta H_{T-e} = \frac{x_{5d1}}{M_{\text{Cr}}} \left[ \frac{1}{2}\Delta H_{\text{Cr}_2\text{O}_3} - \frac{3}{2}\Delta H_{\text{FeO}} - \Delta H_{\text{Cr-S}} + \int_{298}^{T_{\text{isc}}} \frac{3}{2}C_{\text{P,Fe}} + \frac{1}{2}C_{\text{P,Cr}_2\text{O}_3} - \frac{3}{2}C_{\text{P,FeO}} - C_{\text{P,Cr}} dT \right], \quad (31)$$

$$\Delta H_{T-f} = \frac{x_{6d1}}{M_P} \left[ \frac{1}{2}\Delta H_{\text{P}_2\text{O}_5} - \frac{5}{2}\Delta H_{\text{FeO}} - \Delta H_{\text{P-S}} + \int_{298}^{T_{\text{isc}}} \frac{5}{2}C_{\text{P,Fe}} + \frac{1}{2}C_{\text{P,P}_2\text{O}_5} - \frac{5}{2}C_{\text{P,FeO}} - C_{\text{P,P}} dT \right], \quad (32)$$

$$r_P > 0 : \Delta H_{T-h} = \frac{x_{9d5}}{M_{\text{CO}}} \left[ \Delta H_{\text{CO}_2} - \Delta H_{\text{CO}} + \int_{298}^{T_{\text{isc}}} C_{\text{P,CO}_2} - C_{\text{P,CO}} - \frac{1}{2}C_{\text{P,O}_2} dT \right],$$

$$r_P < 0 : \Delta H_{T-h} = \frac{x_{9d3} + x_{9d5}}{M_{\text{CO}}} \left[ \Delta H_{\text{CO}_2} - \Delta H_{\text{CO}} + \int_{298}^{T_{\text{isc}}} C_{\text{P,CO}_2} - C_{\text{P,CO}} - \frac{1}{2}C_{\text{P,O}_2} dT \right], \quad (33)$$

$$\Delta H_{T-i} = \frac{x_{1d4} + x_{1d6} + x_{2d5}}{M_C} \left[ \Delta H_{\text{CO}_2} - \Delta H_{\text{C-S}} + \int_{298}^{T_{\text{isc}}} C_{\text{P,CO}_2} - C_{\text{P,C}} - C_{\text{P,O}_2} dT \right], \quad (34)$$

$$\Delta H_{T-k} = \frac{x_{3d3}}{M_{\text{Si}}} \left[ \Delta H_{\text{SiO}_2} + \Delta H_{\text{SiO}_2-s} - 2\Delta H_{\text{MnO}} - \Delta H_{\text{Si-S}} + \int_{298}^{T_{\text{isc}}} 2C_{\text{P,Mn}} + C_{\text{P,SiO}_2} - C_{\text{P,Si}} - 2C_{\text{P,MnO}} dT \right], \quad (35)$$

$$\Delta H_{T-l} = \frac{x_{3d2}}{M_{\text{Si}}} \left[ \Delta H_{\text{SiO}_2} + \Delta H_{\text{SiO}_2-s} - \Delta H_{\text{Si-S}} + \int_{298}^{T_{\text{isc}}} C_{\text{P,SiO}_2} - C_{\text{P,Si}} - C_{\text{P,O}_2} dT \right], \quad (36)$$

$$\Delta H_{T-m} = \frac{x_{5d2}}{M_{\text{Cr}}} \left[ \frac{1}{2}\Delta H_{\text{Cr}_2\text{O}_3} - \Delta H_{\text{Cr-S}} + \int_{298}^{T_{\text{isc}}} \frac{1}{2}C_{\text{P,Cr}_2\text{O}_3} - C_{\text{P,Cr}} - \frac{3}{4}C_{\text{P,O}_2} dT \right], \quad (37)$$

$$\Delta H_{T-p} = \frac{\dot{m}_{\text{comb}}}{M_{\text{C}_9\text{H}_{20}}} \left[ 9\Delta H_{\text{CO}_2} + 10\Delta H_{\text{H}_2\text{O}} - \Delta H_{\text{C}_9\text{H}_{20}} + \int_{298}^{T_{\text{gas}}} 9C_{\text{P,CO}_2} + 10C_{\text{P,H}_2\text{O}} - C_{\text{P,C}_9\text{H}_{20}} - 14C_{\text{P,O}_2} dT \right], \quad (38)$$

$$\Delta H_{T-q} = \frac{x_{4d4}}{M_{\text{Mn}}} \left[ \Delta H_{\text{MnO}} - \Delta H_{\text{Mn-S}} + \int_{298}^{T_{\text{isc}}} C_{\text{P,MnO}} - C_{\text{P,Mn}} - \frac{1}{2}C_{\text{P,O}_2} dT \right], \quad (39)$$

Total chemical energy without the energy provided by the gas burners, post combustion energy, and carbon monoxide oxidation with leak air energy is assumed to be

transferred to liquid scrap and liquid slag as described by Equation 40.

$$Q_{\text{Chemical Energy-ISC and ISI}} = \sum_{Y=a}^p \Delta H_{T-Y} \quad \text{where } Y \neq h \text{ and } n. \quad (40)$$

Chemical energy of post combustion and carbon monoxide oxidation with leak air is considered to be transferred to liquid slag and gas zone, as described by Equation 33. In the following,  $Q_{\text{CO Post Combustion}}$  shows the chemical energy released due to CO post combustion.

### 2.3.4. Slag Quality

Slag has many useful properties such as insulating the steel bath and, thus, preventing oxidation, reducing heat losses, arc noise, and protecting the refractories from the arc flare and radiation.<sup>[10]</sup> In order to achieve the beneficiary effects of the slag, the slag must have certain characteristics such as appropriate basicity, height, and foaminess.

**2.3.4.1. Slag Basicity:** Chemical compositions of the furnace refractories are usually alkaline. During smelting and refining, acid oxides, such as  $\text{Al}_2\text{O}_3$ ,  $\text{SiO}_2$ , and  $\text{FeO}$  are formed, which erode the refractories. In order to neutralize the acids, calcium lime and dolomite lime are usually added.<sup>[11]</sup> Some indices have been introduced to measure slag basicity using Equation 41.<sup>[12]</sup>

$$\begin{aligned} B_2 &= \frac{m_{\text{CaO}}}{m_{\text{SiO}_2}}, \\ B_3 &= \frac{m_{\text{CaO}}}{m_{\text{SiO}_2} + m_{\text{Al}_2\text{O}_3}}, \\ B_4 &= \frac{m_{\text{CaO}} + m_{\text{MgO}}}{m_{\text{SiO}_2} + m_{\text{Al}_2\text{O}_3}}, \\ B_5 &= \frac{m_{\text{CaO}} + m_{\text{MgO}}}{m_{\text{SiO}_2}}, \end{aligned} \quad (41)$$

**2.3.4.2. Foamy Slag Height:** Foamy slag introduces many advantages, such as bath heat loss reduction, CO retention (better combustion), and roof/wall protection from the arc radiation.<sup>[11]</sup> Additionally to slag basicity, one of the measures to quantify the slag quality, is the foam index. The foam index has a unit of time and represents the time needed in order for the gas to pass through the slag. Several studies have investigated foam index and each of them uses special empirical formulae to describe it. In the present paper, equation based on ref.[11] is used and Equation 42 is considered for slags containing CaO,  $\text{SiO}_2$ , FeO and  $\text{Al}_2\text{O}_3$ :

$$\Xi = \frac{\eta^{1.2}}{\sigma^{0.2} \rho D_B^9}, \quad (42)$$

where  $\eta$  is slag viscosity,  $\sigma$  is surface tension,  $\rho$  is slag density and  $D_B$  is bubble diameter. Parameters used in Equation 42 are calculated using Equation 43–45.

Slag density ( $\text{kg m}^{-3}$ ) and surface tension ( $\text{mN m}^{-1}$ ) can be computed by Equation 43 and 44, respectively.<sup>[13]</sup>

$$\rho = 2460 + 1800 \left( \frac{m_{\text{FeO}}}{m_{\text{Slag}}} + \frac{m_{\text{MnO}}}{m_{\text{Slag}}} \right), \quad (43)$$

$$\sigma = 754.24 - 569.4 \left( \frac{m_{\text{SiO}_2}}{m_{\text{Slag}}} \right) - 137.13 \left( \frac{m_{\text{FeO}}}{m_{\text{Slag}}} \right). \quad (44)$$

Bubble diameter is assumed as a function of slag density and surface tension. In this model, surface fitting was used to obtain the appropriate equation with data of slag density and slag surface tension<sup>[14]</sup> as described by Equation 45 in (mm):

$$\begin{aligned} D_B &= [25.34 + 9.28\bar{\rho} - 18.74\bar{\sigma} - 162.06\bar{\rho}^2 \\ &\quad + 329.95\bar{\rho}\bar{\sigma} - 173.18\bar{\sigma}^2 + 106.77\bar{\rho}^2\bar{\sigma} - 239.39\bar{\rho}\bar{\sigma}^2 \\ &\quad + 137.73\bar{\sigma}^3], \bar{\sigma} = \frac{\sigma - 362.3}{163.1}, \bar{\rho} = \frac{\rho - 2436}{639.7}, \end{aligned} \quad (45)$$

Slag height is obtained by multiplying superficial velocity by foam index as shown in Equation 57 described in ref.[6] The superficial gas velocity [ $V_g$ ] is determined by dividing the volume change rate by the EAF area in Equation 46:

$$V_g = \frac{\left[ \left( \frac{1}{M_{\text{CO}}} \times 9_{d2} \right) R_{\text{gas}} T_{\text{ISI}} \right]}{[(r_p + a_p) \Pi r_{\text{EAF}}^2]}, \quad (46)$$

where  $R_{\text{gas}}$  is the universal gas constant,  $r_{\text{EAF}}$  is radius of the EAF and  $a_p$  is the atmospheric pressure.

## 2.4. Heat Transfer Module

Heat transfer module consists of four main parts: heat transfer coefficient module, radiative heat transfer module, reference energy system and mass/temperature rate calculation. Relations between all four parts of the model can be seen in Figure 2.

### 2.4.1. Hot Heel

Most of the modern EAFs use hot heel technique, as it directly influences EAF productivity (tones (h MW)<sup>-1</sup>), power-on time, energy consumption, reduces flickers, decreases furnace wear, and damage probability.<sup>[15–17]</sup> Many studies investigated what is the proper amount of hot heel for optimal EAF operation. Rathaba<sup>[15]</sup> reports that hot heel amount should be less than 10% of the total charge. Furthermore, Arzpeyma<sup>[16]</sup> reports that hot hell amount should be in the range of 15–20.0% of the charge.

Finally, Memoli et al.,<sup>[17]</sup> who investigated the influence of hot heel amount on productivity, power-on time, and energy consumption, showed that optimum hot heel amount should be in the range of 55–60% of the tapping size, which ensures maximum productivity and energy efficiency.

#### 2.4.2. Radiative Heat Transfer

The radiative heat transfer sub-module has been developed to estimate the radiation losses, which originate from arc (arc), the lower-wall zone or refractory brick (wall), upper-wall zone or water-cooled panels (water), roof zone (roof), electrode zone (electrode) and liquid slag zone (ISL). The role of the arcs, considering the radiation losses, is described in Section 2.4.3.

All zones (except the arc) are assumed as gray bodies and all the equations follow the related assumption stated in Section 2.1. Equation 47 describes the radiosity of each surface, while the radiative loss of each zone is obtained by Equation 48. In the case that the slag has not been formed yet, solid scrap zone is substituted for liquid slag zone in the equations.

$$(J_i - \sigma_B T_i^4) \frac{NA_i \varepsilon_i}{1 - \varepsilon_i} + \sum_{j \neq i} [(J_i - J_j) NA_i F_{ij}] = 0, \quad (47)$$

$$Q_{Rad_{i-j}} = (J_i - J_j) NA_i VF_{i-j} \quad (48)$$

where  $VF_{i-j}$  is view factor between surface  $i$  and  $j$ ,  $\varepsilon_i$  is surface emissivity  $i$ ,  $\sigma_B$  is Stefan–Boltzman constant,  $J_i$  is radiosity of zone  $i$ ,  $NA_i$  is the area of a surface  $i$  that reaches out of the slag and bath zone that is located inside the EAF.

second, such as increased arc stability<sup>[18]</sup> and lower impact to wall, water, and roof zones in a form of radiative arc energy. On the other hand, increased radiation to wall, water, and roof zones from the slag occurs. Foaminess of the slag is determined by the foaming index (Equation 42) and depends on its viscosity and surface tension. In general, proper foaminess of the slag leads to lower energy consumption as more energy is transferred to the steel, instead to the walls, roof, and water-cooled panels.

Since slag properties, slag height, arc length, arc power, zone temperatures, and bath height vary during the heat, the amounts of radiative heats between the zones need to be calculated in each computational step.

#### 2.4.3. Reference Energy System (RES)

For easier and more accurate evaluation of the model, the EAF has been divided into eleven zones, i.e., arc zone (arc), solid scrap zone (sSc), liquid scrap zone (lSc), solid slag zone (sSl), liquid slag zone (lSl), gas zone (gas), electrode zone (electrode), floor zone (floor), lower-wall zone or refractory brick (wall), upper-wall zone or water-cooled panels (water), and roof zone (roof).

In a case of EAF being charged with scrap, additives and slag materials in discrete moments, each material charging event is equivalent to addition of one zone; sSc or sSl, respectively, and is represented with 2 own state variables, i.e., temperature and mass of the solid form. Before charging the baskets, their energy changes are equal to zero; therefore, their own state variables (mass and temperature) are fixed.

During each batch, the changes in arc lengths, slag height, and scrap height can cause seven possible states, such as:

A	$L_{lSc} + L_{sSc} + L_{lSl} + L_{sSl} > L_{wall}$ ,	$L_{arc} > L_{lSl} + L_{sSl}$	$L_{arc} + L_{lSc} + L_{sSc} > L_{wall}$
B	$L_{lSc} + L_{sSc} + L_{lSl} + L_{sSl} < L_{wall}$ ,	$L_{arc} > L_{lSl} + L_{sSl}$	$L_{arc} + L_{lSc} + L_{sSc} < L_{wall}$
C	$L_{lSc} + L_{sSc} + L_{lSl} + L_{sSl} < L_{wall}$ ,	$L_{arc} = L_{lSl} + L_{sSl}$	$L_{arc} + L_{lSc} + L_{sSc} < L_{wall}$
D	$L_{lSc} + L_{sSc} + L_{lSl} + L_{sSl} > L_{wall}$ ,	$L_{arc} = L_{lSl} + L_{sSl}$	$L_{arc} + L_{lSc} + L_{sSc} > L_{wall}$
E	$L_{lSc} + L_{sSc} + L_{lSl} + L_{sSl} < L_{wall}$ ,	$L_{arc} > L_{lSl} + L_{sSl}$	$L_{arc} + L_{lSc} + L_{sSc} > L_{wall}$
F	$L_{lSc} + L_{sSc} + L_{lSl} + L_{sSl} < L_{wall}$ ,	$L_{arc} < L_{lSl} + L_{sSl}$	$L_{arc} + L_{lSc} + L_{sSc} < L_{wall}$
G	$L_{lSc} + L_{sSc} + L_{lSl} + L_{sSl} > L_{wall}$ ,	$L_{arc} < L_{lSl} + L_{sSl}$	

To estimate the necessary view factors, surfaces such as walls, cooling panels, and electrodes are considered to have a cylindrical shape, while the roof and the liquid slag surfaces are considered to have a ring shape. The view factors are extracted from<sup>[19,20]</sup> and are obtained using a reciprocity relation, superposition rule, symmetry rule and a summation rule.

One of the important aspects when computing the radiative heat transfer are properties of the slag covering the bath. Two types of slags are considered, foamy and non-foamy. The first has several advantages over the

In the following, the heat transfer equations for each zone are described considering the above seven possible EAF states.

Convection heat transfer rate is assessed by Newton's law (Equation 49). Heat transfer coefficients are obtained through estimation of the Nusselt number ( $Nu$ ). In the following, Nusselt number equations are suggested for both solid and liquid material forms.

$$Q_{conv\ x-y} = Nu_{x-y} \frac{K_{x-y}}{L_{x-y}} A_{x-y} (T_x - T_y) \quad (49)$$

where  $L_{x-y}$  and  $K_{x-y}$  are the characteristic length of the fluid and thermal conductivity of the fluid (zone  $x$  or  $y$ ),  $A_{x-y}$  denotes a part of the zone area  $x$  facing the zone  $y$ . These variables should be evaluated at each step.

The arc model as presented in ref.[7] is used to obtain the dissipation of the arc energy and is represented by Equation 50–52:

$$P_r = 3\pi r_{CAM}^2 L_{arc} u, \quad (50)$$

$$P_e = 3I_{arc} \left[ O_{an} + \frac{5k_B T_{arc}}{2e} + U_{an} \right], \quad (51)$$

$$P_{conv} = 3\pi R_{arc}^2 \rho_{arc} \bar{v}_k (h_k - h_f), \quad (52)$$

where  $P_r$  represents the radiation power from the arc [W],  $P_e$  is the electron flow power from the arc [W],  $P_{conv}$  is the convective power from the arc [W],  $r_{CAM}$  is the channel arc model radius,  $u$  is arc radiation density [ $W m^{-3}$ ],  $I_{arc}$  is the arc current [A],  $O_{an}$  is the work function for the anode [V],  $k_B$  is the Boltzman constant [ $J K^{-1}$ ],  $T_{arc}$  is the arc temperature [K],  $e$  is the electron charge [J],  $U_{an}$  is the anode voltage drop [V] and  $\rho_{arc}$  is the arc density [ $kg m^{-3}$ ].

Energy balance for each zone can be calculated at any time and in any state according to Table 1. The equations used to calculate energy balance for each zone are presented in Table 5 in the appendix.

Before slag formation, solid scrap interacts with the gas zone, meaning that the energy exchanged between sSc and gas zones [ $Q_{Conv,sSc-gas}$ ] should be considered in energy balance for gas and sSc zones.

In the following, subscriptions  $\xi$  and  $\nu$  along with sSc and sSl, respectively, delineate  $\xi$ th solid scrap and  $\nu$ th solid slag baskets unloaded. It is assumed that EAF can be charged with  $N$  baskets of solid scrap and  $M$  baskets of solid slag.

1.  $Q_{Conv,lSc-sSc_\xi}$  is the energy transferred from lSc to  $\xi$ th sSc basket. The energy transferred to each basket of solid scrap charged is estimated by Equation 49. Heat transfer coefficient is computed by the model presented in ref.[21] The scrap area surrounded by lSc is

$$\text{calculated in each iteration as: } A_{sSc_\xi} = \left[ 6 \left( \frac{m_{sSc_\xi}}{\rho_{sSc_\xi}} \right)^{\frac{2}{3}} \right],$$

where  $\rho_{sSc_\xi}$  is the average scrap density of the  $\xi$ th basket.

2.  $Q_{CH4-sSc_\xi}$  is the energy received from the burners and is calculated by Equation 1 and 3 presented in ref.[5]

3.  $Q_{arc-lSc}$  is the energy transferred to lSc from the arc through electron flow, convection, and radiation as represented by Equation 53. Arc energy transferred to liquid scrap through radiation and convection is proportional to the ratio of the contact area between the electrode ( $[\pi r_{CAM}^2]$ ) and the arc ( $\left[ \frac{r_{CAM}}{2r_{CAM} + 2L_{arc}} \right]$ ):

$$Q_{arc-lSc} = \left[ \frac{r_{CAM}}{2r_{CAM} + 2L_{arc}} (P_r + P_{conv}) + P_e \right] \quad (53)$$

4.  $Q_{chem-lSc}$  is the chemical energy transferred to lSc and is represented by Equation 54. It is assumed that chemical energy is transferred to the liquid scrap and liquid slag zones.

$$Q_{chem-lSc} = \varphi_{Chemical\ Energy-lSc} Q_{Chemical\ Energy-lSc\ and\ lSl} \quad (54)$$

where  $\varphi_{Chemical\ Energy-lSc}$  is a fraction of chemical energy transferred to lSc.

5.  $Q_{CH4-lSc}$  is the energy transferred from the burners to the lSc zone and is obtained by Equation 3 and 9 presented in ref.[5]

6.  $Q_{Conv,lSc-lSl}$  is the energy transferred from the lSc to lSl, where liquid slag velocity is assumed to be zero,<sup>[22]</sup> i.e., slag is considered as a solid surface. The Nusselt number is calculated by Equation 55.<sup>[23]</sup> The same equation is used to predict heat transfer coefficient of  $Q_{Conv,lSc-floor}$ ,  $Q_{Conv,lSl-gas}$ ,  $Q_{Conv,sSc-gas}$  and  $Q_{Conv,gas-roof}$ . If the fluid is gas, Equation 56 is used to compute the Rayleigh number. Flux transferred to the water-cooled panels should be in the permissible range as mentioned in ref.<sup>[24]</sup> to prevent damage of the panels.

$$\begin{aligned} T_{lSc} < T_{lSl} \quad H_1 &= \frac{0.527}{\left[ 1 + \left( \frac{1.9}{Pr} \right)^{0.9} \right]^{\frac{2}{9}}}, \\ \text{Case 1} \quad T_{lSc} > T_{floor} \quad NUT &= H_1 Ra^{0.2} \quad (55a) \\ T_{gas} > T_{lSl} \end{aligned}$$

$$T_{gas} > T_{sSc} \quad Nu = \frac{2.45}{\ln \left( 1 + \frac{2.45}{NUT} \right)}$$

$$T_{gas} < T_{roof}$$

$$\begin{aligned} T_{lSc} > T_{lSl} \quad C_1 &= \frac{0.671}{\left[ 1 + \left( \frac{0.429}{Pr} \right)^{\frac{9}{16}} \right]^{\frac{4}{9}}}, \\ \text{Case 2} \quad T_{lSc} < T_{floor} \quad Nu^T &= 0.835 C_1 Ra^{0.25} \\ T_{gas} < T_{lSl} \quad Nu_1 &= \frac{2.0}{\ln \left( 1 + \frac{1.4}{Nu^T} \right)} \\ T_{gas} < T_{sSc} \quad Nu_t &= C_1^H Ra^{\frac{1}{3}} \\ T_{gas} > T_{roof} \quad Nu &= [Nu_1^{10} + Nu_t^{10}]^{0.1} \quad (55b) \end{aligned}$$

Energy balance				
Involved zones				
Zone	Convection	Radiation	Others	States
sSc	ISc, [gas] <sup>a)</sup>		Gas injection	A–G
ISc	Arc, ISl, sSc wall, floor	Arc	Gas injection, Chemical reaction, HBI/DRI injected	A–G
sSl	ISl			A–G
ISl	Arc, sSl, ISc, gas, wall, water, electrode	Arc, water, electrode, roof	Chemical reaction, Post combustion	G
	Arc, sSl, ISc, gas, wall, water	Arc, water, electrode, roof		A, D
	Arc, sSl, ISc, gas, wall, electrode	Arc, water, electrode, roof, wall		F
	Arc, sSl, ISc, gas, wall,	Arc, water, electrode, roof, wall		B, C, E
Gas	Arc, ISl or sSc <sup>a)</sup> , roof, water, wall, electrode		Post combustion, Off gas, Leakage, Hatch, Oxygen injected (main and post), Gas injection	B, E
	ISl, roof, water, wall, electrode			C, F
	arc, ISl or sSc <sup>a)</sup> , roof, water, electrode			A
	ISl, roof, water, electrode			D, G
Electrode	Arc, gas, ISl	Arc, ISl, water, wall, roof	Ohmic	F
	Arc, gas	Arc, ISl, water, wall, roof		B, C
	Arc, gas, ISl,	Arc, ISl, water, roof		G
	Arc, gas	Arc, ISl, water, roof		A, D, E
Water	ISc, gas	Arc, ISl, electrode, roof		A
	Gas	Arc, ISl, wall, electrode, roof		E
	ISc, gas	ISl, electrode, roof		D, G
	Gas	Wall, electrode, ISl, roof		B, C, F
Wall	ISc, ISl, gas	Arc, electrode, water, roof, ISl		B, E
	ISc, ISl, gas,	Electrode, water, roof, ISl		C, F
	ISc, ISl			A, D, G

Table 1. Continued

## Energy balance

Involved zones				
Zone	Convection	Radiation	Others	States
roof	gas	lSl, electrode, wall, water		B, C, E, F
	gas	lSl, electrode, water		A, D, G
floor	lSc			A–G

a) Before slag formation.

**Table 1.** Energy balance for EAF zones.

where  $K$  is thermal conductivity of the fluid,  $Ra$  and  $Pr$  represent the Rayleigh number and the Prandtl number.

$$Gr = \frac{g\beta(|T_{\text{gas}} - T_x|)(2r_{\text{EAF}})^3}{\left(\sum_{i=\text{CO,CO}_2 \text{ and N}_2} \frac{N_i}{N_{\text{CO}} + N_{\text{CO}_2} + N_{\text{N}_2}} v_i\right)^2},$$

$$Pr = \frac{\left(\sum_{i=\text{CO,CO}_2 \text{ and N}_2} \frac{N_i}{N_{\text{CO}} + N_{\text{CO}_2} + N_{\text{N}_2}} \mu_i\right) \left(\sum_{i=\text{CO,CO}_2 \text{ and N}_2} \frac{N_i}{N_{\text{CO}} + N_{\text{CO}_2} + N_{\text{N}_2}} C_i\right)}{\sum_{i=\text{CO,CO}_2 \text{ and N}_2} \frac{N_i}{N_{\text{CO}} + N_{\text{CO}_2} + N_{\text{N}_2}} K_i},$$

where  $N_i$  is the number of the  $i$  gas mole in gas,  $T_x$  is zone temperature (roof, electrodes, wall, or lSl),  $g$  is the gravity [ $\text{m s}^{-2}$ ],  $\beta$  is the volume coefficient of expansion [ $1 \text{ K}^{-1}$ ],  $\nu$  is the kinematic viscosity [ $\text{m}^2 \text{ s}^{-1}$ ],  $\mu$  is the dynamic viscosity [ $\text{kg (ms)}^{-1}$ ],  $C$  is the specific heat [ $\text{J (kg K)}^{-1}$ ], and  $K$  is the thermal conductivity of fluid [ $\text{W (mK)}^{-1}$ ].

1.  $Q_{\text{Conv}_{\text{lSc-wall}}}$  describes the energy transferred from lSc to the wall. The Nusselt number is obtained by Equation 57.<sup>[23]</sup> This  $Nu$  can be used to obtain  $Q_{\text{Conv}_{\text{lSl-wall}}}$ ,  $Q_{\text{Conv}_{\text{lSl-water}}}$ ,  $Q_{\text{Conv}_{\text{gas-water}}}$ , and  $Q_{\text{Conv}_{\text{gas-wall}}}$ :

$$Nu = \left[ \left(\frac{Ra}{16}\right)^{-1} + (0.8Ra^{0.25})^{-1} \right]^{-1},$$

2.  $Q_{\text{lSc-HBI}}$  represents the energy required to melt the HBI and to reach the desired bath temperature. Equation 58 describes the energy exchange between the liquid scrap and HBI:

$$Q_{\text{lSc-HBI}} = \dot{m}_{\text{HBI}} \left[ \int_{T_{\text{HBI}}}^{T_{\text{lSc}}} C_{\text{p,Fe}} dt + \lambda_{\text{Fe}} \right],$$

where  $\dot{m}_{\text{HBI}}$  is the HBI injection flow [ $\text{kg s}^{-1}$ ].

3.  $Q_{\text{Conv}_{\text{lSl-slv}}}$  represents the energy transferred from the lSl to  $v$ th charged solid slag basket. The energy

transferred to each solid slag basket is obtained by Equation 6 presented in ref.[5]

4.  $Q_{\text{arc-lSl}}$  represents the energy transferred from the arc to lSl. It is assumed that the arc energy is transferred to the liquid slag through radiation and convection mechanisms as described by Equation 59 and is proportional to the ratio of the common area between the arc and slag, to arc area depicted by  $\left[\frac{h_{\text{arc-lSl}}}{r_{\text{CAM}} + L_{\text{arc}}}\right]$ :

$$Q_{\text{arc-lSl}} = \frac{h_{\text{arc-lSl}}}{r_{\text{CAM}} + L_{\text{arc}}} (P_r + P_{\text{conv}}),$$

5.  $Q_{\text{chem-lSl}}$  represents the chemical energy transferred to the lSl calculated by Equation 60:

$$Q_{\text{chem-lSl}} = (1 - \varphi_{\text{Chemical Energy-lSc}}) Q_{\text{Chemical Energy-lSc and lSl}},$$

6.  $Q_{\text{CO Post-lSl}}$  represents the share of the CO post-combustion energy that is transferred to lSl and depends on the efficiency  $K_{\text{Post}}$ , obtained by Equation 61:

$$Q_{\text{CO Post Combustion-lSl}} = K_{\text{post}} Q_{\text{CO Post Combustion}},$$

7.  $Q_{\text{lSl-electrode}}$  describes the energy transferred from the lSl to the electrode through convection and radiation mechanisms. Amount of energy exchanged through radiation mechanism is estimated by Equation 47

and 48. In order to calculate the transferred energy through convection mechanism, the Nusselt number is calculated by Equation 62<sup>[25]</sup> and 63 dependent on the Reynolds number. The  $Nu$  can be employed for  $Q_{\text{conv gas-electrode}}$ .

$$Nu = 0.59Ra^{0.25}, \quad (62)$$

$$Nu = \frac{4}{3} \left[ \frac{7 Gr Pr^2}{5(20 + 21 Pr)} \right]^{0.25} + \left[ 4(272 + 315 Pr) \frac{h_{\text{electrode-x}}}{35 D_{\text{electrode}} (64 + 63 Pr)} \right], \quad (63)$$

where  $D_{\text{electrode}}$  is the equivalent electrode diameter and  $h_{\text{electrode-x}}$  is the length of the electrode facing zone  $x$  (gas or ISL).

8.  $Q_{\text{Conv arc-gas}}$  represents the arc energy transferred to gas thorough convection as described by Equation 64. The part of the arc energy that is transferred by convection to gas has a direct relation with the arc length that contacts the gas.

$$Q_{\text{Conv arc-gas}} = \frac{h_{\text{arc-gas}}}{r_{\text{CAM}} + L_{\text{arc}}} P_{\text{conv}}, \quad (64)$$

9.  $Q_{\text{CO Post-gas}}$  represents a part of the CO post-combustion energy that is transferred to gas and is computed similarly as in Equation 19 presented in ref.<sup>[15]</sup>
10.  $Q_{\text{CH}_4\text{-gas}}$  represents the energy received from the gas burners and is approximated by Equation 65:

$$Q_{\text{CH}_4\text{-gas}} = \Delta H_{\text{T-n}} - \left( \sum_{\xi=1}^N Q_{\text{CH}_4\text{-sSc}_\xi} + Q_{\text{CH}_4\text{-ISc}} \right). \quad (65)$$

11.  $Q_{\text{O}_2\text{-Stream Injection}}$  represents the heat loss to oxygen in the stream and is approximated by Equation 66:

$$Q_{\text{O}_2\text{-Stream Injection}} = - \left( \frac{d_1}{M_{\text{O}_2}} \right) \int_{T_{\text{O}_2\text{-Stream Injection}}}^{T_{\text{gas}}} C_{\text{P-O}_2}(T) dT, \quad (66)$$

where  $d_1$  is oxygen lancing rate ( $\text{kg s}^{-1}$ ) and  $T_{\text{O}_2\text{-Stream Injection}}$  is temperature of oxygen.

12.  $Q_{\text{O}_2\text{-Post}}$  represents the heat loss to oxygen for the post combustion and is approximated by Equation 67:

$$Q_{\text{O}_2\text{-Post}} = - \left( \frac{d_6}{M_{\text{O}_2}} \right) \int_{T_{\text{O}_2\text{-Post Stream Injection}}}^{T_{\text{gas}}} C_{\text{P-O}_2}(T) dT, \quad (67)$$

where  $d_6$  is oxygen post-combustion flow ( $\text{kg s}^{-1}$ ) and  $T_{\text{O}_2\text{-Post Stream Injection}}$  is temperature of the oxygen injected for post combustion.

13.  $Q_{\text{Off Gas}}$  represents the heat loss to  $\text{N}_2$ , CO, and  $\text{CO}_2$  in the off gas and is approximated by Equation 68:

$$Q_{\text{Off Gas}} = - \left( \frac{x11d1}{M_{\text{N}_2}} \right) \int_{T_{\text{Air}}}^{T_{\text{gas}}} C_{\text{P-N}_2}(T) dT - \left( \frac{x9d1}{M_{\text{CO}}} \right) \int_{T_{\text{Air}}}^{T_{\text{gas}}} C_{\text{P-CO}}(T) dT - \left( \frac{x10d1}{M_{\text{CO}_2}} \right) \int_{T_{\text{Air}}}^{T_{\text{gas}}} C_{\text{P-CO}_2}(T) dT \quad (68)$$

where  $T_{\text{Air}}$  is the outdoor air temperature.

14.  $Q_{\text{Leak Air}}$  represents the heat loss to  $\text{N}_2$  and  $\text{O}_2$  in leak air obtained by Equation 69:

$$Q_{\text{Leak Air}} = - \left( \frac{x11d2}{M_{\text{N}_2}} \right) \int_{T_{\text{Air}}}^{T_{\text{gas}}} C_{\text{P-N}_2}(T) dT - \left( \frac{x12d2}{M_{\text{O}_2}} \right) \int_{T_{\text{Air}}}^{T_{\text{gas}}} C_{\text{P-O}_2}(T) dT, \text{ if } r_p < 0. \quad (69)$$

15.  $Q_{\text{hatch}}$  represents the heat loss to  $\text{N}_2$ , CO, and  $\text{CO}_2$  in the hatches. It occurs, if  $r_p > 0$  and is calculated by Equation 70:

$$Q_{\text{hatch}} = - \left( \frac{x11d3}{M_{\text{N}_2}} \right) \int_{T_{\text{Air}}}^{T_{\text{gas}}} C_{\text{P-N}_2}(T) dT - \left( \frac{x9d4}{M_{\text{CO}}} \right) \int_{T_{\text{Air}}}^{T_{\text{gas}}} C_{\text{P-CO}}(T) dT - \left( \frac{x10d7}{M_{\text{CO}_2}} \right) \int_{T_{\text{Air}}}^{T_{\text{gas}}} C_{\text{P-CO}_2}(T) dT. \quad (70)$$

16.  $Q_{\text{ohmic}}$  represents the ohmic loss described by Equation 71:

$$Q_{\text{Ohmic}} = 3 R_{\text{electrode}} I_{\text{arc}}^2, \quad (71)$$

where  $R_{\text{electrode}}$  is the electrode resistance [ $\Omega$  electrode<sup>-1</sup>].

17.  $Q_{\text{arc-electrode}}$  represents the arc energy transferred to electrode through convection and radiation as described by Equation 72. The value is proportional to the common area between the electrode ( $[\pi r_{\text{CAM}}^2]$ ) and the arc ( $\left[ \frac{r_{\text{CAM}}}{2r_{\text{CAM}} + 2L_{\text{arc}}} \right]$ ):

$$Q_{\text{arc-electrode}} = \frac{r_{\text{CAM}}}{2r_{\text{CAM}} + 2L_{\text{arc}}} (P_r + P_{\text{conv}}), \quad (72)$$

18.  $Q_{\text{Rad arc-water}}$  represents the arc energy transferred to water. It has a direct relation with the arc length that faces the water. This assumption is based on the results presented in ref.[26] The radiated energy is determined by Equation 73:

$$Q_{\text{Rad}_{\text{arc-water}}} = \frac{h_{\text{arc-water}}}{r_{\text{CAM}} + L_{\text{arc}}} P_{\text{T}}, \quad (73)$$

19.  $Q_{\text{Rad}_{\text{arc-wall}}}$  represents the arc energy transferred to wall. It has a direct relation with the arc length that faces the wall. This assumption based on the results presented in ref.[26] The radiated energy is determined by Equation 74:

$$Q_{\text{Rad}_{\text{arc-wall}}} = \frac{h_{\text{arc-wall}}}{r_{\text{CAM}} + L_{\text{arc}}} P_{\text{T}}, \quad (74)$$

#### 2.4.4. State Variables of the Heat-Transfer Module

The rates of change of temperature and mass of elements and compounds are calculated using the rate of thermal energy. For calculating these rates, the zones considered in this model can be classified into three groups, i.e., (i) zones in which both temperature and mass change during the batch (sSc, lSc, sSl, lSl, and electrode); (ii) zones in which only the temperature changes (i.e., floor, wall, and gas); and (iii) zones in which both temperature and mass are constant (roof, water, and arc).

##### 2.4.4.1. First Group

**2.4.4.1.1. Rate of Change of Scrap Mass/Temperature:** The rate of melting and heating of charged solid scrap baskets are defined by Equation 75 and 76, respectively, which are the modified equations defined in the previous model.

$$\dot{m}_{\text{sSc}_{\xi}} = - \frac{Q_{\text{sSc}_{\xi}} \left( \frac{T_{\text{sSc}_{\xi}}}{T_{\text{lSc}}} \right)}{\lambda_{\text{sSc}} + \left( \int_{T_{\text{sSc}_{\xi}}}^{T_{\text{lSc}}} C_{\text{p,Fe}}(T) dT \right)}, \quad (75)$$

$$\dot{T}_{\text{sSc}_{\xi}} = \frac{Q_{\text{sSc}_{\xi}} \left( 1 - \frac{T_{\text{sSc}_{\xi}}}{T_{\text{lSc}}} \right)}{m_{\text{sSc}_{\xi}} C_{\text{p,Fe}}(T_{\text{sSc}_{\xi}})}. \quad (76)$$

**2.4.4.1.2. Rate of Change of Liquid Mass/Temperature:** The rate of change of liquid scrap mass is a function of chemical reactions, the heat transferred to the solid scrap zones and additives as described by Equation 77:

$$\begin{aligned} \dot{m}_{\text{lSc}} &= \sum_{\xi=1}^N \dot{m}_{\text{sSc}_{\xi}} + \sum_i \dot{m}_i - \sum_{\text{add}} \sum_i C_{\text{add}_i} \dot{m}_{\text{add}}, \\ i &= \text{Fe, Si, Mn, Cr, P, add} \\ &= \text{FeMn, FeSi, AlLi, Coke, Carburit} \end{aligned} \quad (77)$$

where the first part of the equation  $\left( -\sum_{\xi=1}^N \dot{m}_{\text{sSc}_{\xi}} \right)$  indicates the summation of the melting rate of scrap baskets, while

second part  $\left( \sum_i \dot{m}_i \right)$  indicates the rate of change of elements in the bath due to chemical reactions. The third part  $\left( -\sum_{\text{add}} \sum_i C_{\text{add}_i} \dot{m}_{\text{add}} \right)$  represents the change of elements due to melting of the additives and releasing of the elements into the bath zone,  $C_{\text{add}_i}$  is the percentage of element  $i$  in addition add.

The rate of change of liquid temperature is approximated by Equation 78:

$$\dot{T}_{\text{lSc}} = \frac{Q_{\text{lSc}}}{m_{\text{lSc}} C_{\text{p,Fe}}(T_{\text{lSc}})}, \quad (78)$$

**2.4.4.1.3. Rate of Change of Solid Slag Mass/Temperature:** Melting and heating rate of solid slag are calculated by equations similar to Equation 75 and 76, respectively.

**2.4.4.1.4. Rate of Change of Liquid Slag Mass/Temperature:** The rate of change of liquid slag mass can be described by equation similar to Equation 77 and the rate of change of liquid slag temperature is calculated by Equation 79:

$$\begin{aligned} \dot{T}_{\text{lSl}} &= \frac{Q_{\text{lSl}} - \left[ \sum_{i=1}^5 \left[ \left( \int_{T_{\text{chem}}}^{T_{\text{lSl}}} C_{\text{p},i}(T) dT \right) (\dot{m}_i) \right] \right]}{\left( m_{\text{lSl}} - \sum_{i=1}^5 m_i \right) C_{\text{p,slag}}(T_{\text{lSl}}) + \sum_{i=1}^5 m_i C_{\text{p},i}(T_{\text{lSl}})} \\ i &= \text{FeO, SiO}_2, \text{P}_2\text{O}_5, \text{Cr}_2\text{O}_3, \text{ and MnO}, \end{aligned} \quad (79)$$

where  $T_{\text{chem}}$  is the reaction temperature.

**2.4.4.1.5. Rate of Change of Electrode Mass/Temperature:** The rate of change of electrode mass is considered as a function of chemical reactions indicated by Equation 80, while the rate of change of electrode temperature is calculated by Equation 81. Since these rates are negligible in comparison to its mass they may be assumed constant during the operation.

$$\frac{dm_{\text{electrode}}}{dt} = -x_{2d6} - 3 \left[ R_{\text{tip}} \frac{I_{\text{arc}}^2}{3600} + R_{\text{side}} \frac{A_{\text{side}}}{3600} \right], \quad (80)$$

$$\frac{dT_{\text{electrode}}}{dt} = \frac{Q_{\text{electrode}}}{m_{\text{electrode}} C_{\text{p,electrode}}}, \quad (81)$$

where  $m_{\text{electrode}}$  is the equivalent mass of three electrodes.

**2.4.4.2. Second Group:** Energy exchange in wall/floor/gas only affects the corresponding temperature change as described by Equation 82–84:

$$\frac{dT_{\text{wall}}}{dt} = \frac{Q_{\text{wall}}}{m_{\text{wall}} C_{P,\text{wall}}}, \quad (82)$$

$$\frac{dT_{\text{floor}}}{dt} = \frac{Q_{\text{floor}}}{m_{\text{floor}} C_{P,\text{floor}}}, \quad (83)$$

$$\frac{dT_{\text{gas}}}{dt} = \frac{Q_{\text{gas}}}{\sum_{i=1}^3 m_i C_{P,i}} \quad i = \text{N}_2, \text{CO}, \text{and } \text{CO}_2. \quad (84)$$

**2.4.4.3. Rates of Change of Elements/Compounds:** The rate of change of elements/compounds is a function of chemical reactions, material injection, and material fusion. The fusion of the scrap and additive materials results in a change of masses of the corresponding elements/compounds, where the melting rates are proportional to the melting rate of scrap and additive materials as described by Equation 85 and 86, respectively (according to the assumptions expressed in section 2.1.). The slag forming materials and the additives supported by the model are brick, lime, dolomite, carburit, FeMn, FeSi, SiMn, Al, and coke.

The model considers ingredients in each scrap basket such as C, Si, S, P, Al, Mn, Cr, and combustible materials and also ingredients in each slag basket such as ash, C, S, Si, Mn, Al, Al<sub>2</sub>O<sub>3</sub>, SiO<sub>2</sub>, MgO, and CaO.

$$\dot{m}_{\text{Fusion } i} = -\sum_{\xi=1}^n C_{s\text{Sc}_{\xi}} \dot{m}_{s\text{Sc}_{\xi}} + C_{\text{HBI}_i} \dot{m}_{\text{HBI}_i}, \quad (85)$$

$i = \text{C, Si, P, Al, Mn, and Cr,}$

$$\dot{m}_{\text{Fusion } j} = -\sum_{v=1}^M C_{s\text{Sl}_v} \dot{m}_{s\text{Sl}_v} - \sum_{\text{add}} C_{\text{add}_j} \dot{m}_{\text{add}_j},$$

$j = \text{Ash, C, S, Si, Mn, Al, Al}_2\text{O}_3, \text{SiO}_2, \text{MgO, and CaO}$

$\text{add} = \text{carburit, FeMn, FeSi, SiMn, Al, and coke}$  (86)

where  $\dot{m}_{\text{Fusion } i}$  is the rate of change of element  $i$  in liquid scrap due to fusion,  $C_{s\text{Sc}_{\xi}}$  is the percentage of element  $i$  in  $\xi$ th solid scrap basket,  $C_{\text{HBI}_i}$  is the share of element  $i$  in HBI,  $\dot{m}_{\text{Fusion } j}$  is the rate of change of element/compound  $j$  due to fusion,  $C_{\text{add}_j}$  is the share of element/compound  $j$  in additive,  $\dot{m}_{\text{add}}$  is the melting rate of additive material add and  $C_{s\text{Sl}_v}$  is the share of element/compound  $j$  in  $v$ th solid slag basket.

For computing the total rate of change of elements/compounds, these values are added to relevant variables that have been estimated with appropriate equations stated in Section 2.3.1.

### 3. Results and Validation

Validation of the model has been performed using the operational measurements of the EAF. The measured EAF

data is used to validate the model-estimated values and overall accuracy of the model. The model is solved using the implicit Adams–Bashforth–Moulton (ABM) predictor–corrector method,<sup>[27]</sup> which is used due to its advantages of both explicit and implicit methods.<sup>[28]</sup> Initial points required for the ABM method are determined by the Euler method. Time step for integration is determined by an adaptive method, which changes the time step in order to assure proper calculation time, accuracy and stability of the method. The adaptation of the step is done in the following cases. First, when a rapid change of state or algebraic variable is observed (especially when it is close to zero) and second, when one of the variables is close to zero. In these two cases, a time step is reduced, simulation is shifted a few samples back and started from that point on. Whether any of the cases is detected again, the time step is reduced one more time. The procedure can shorten the time step to a predefined minimum value. When the numerical issues are resolved, the time step is restored to its initial value. The other feature of the model, which eliminates the need to reduce the time step, is to consider discrete inputs as continuous in a very short time span. In this manner, variables or states do not change instantly and do not cause numerical issues.

Properties of compounds and elements such as specific heat, thermal conductivity, density etc. used in the model can be obtained from different publications such as.<sup>[5,6,14,29]</sup> Compositions of materials in additives and elements in scraps are not constant and are evaluated based on the experimental data.

In the present study, different batches of a 105 ton EAF with an 85 MVA transformer have been used for model parameterization and validation; however, only four of them are presented here. Since the case study is based on an industrial furnace, the samples are taken only at the end of the melting stage (to add alloys according to the oxygen and carbon content) and at the end of the refining stage (to reach final bath quality and temperature). Thus, using data from an industrial furnace has many advantages as well as some drawbacks when validating the model. One of the drawbacks is certainly non-uniformity of the bath, which influences the sampling performed using a lance with special disposable probes. Since the model assumes uniform bath conditions, deviations between measured and simulated values are expected; however, using additional calculations based on energy balance, it has to be clear whether the deviations arise from model inaccuracy or measurement flaws.

In the following, validation results based on temperature and composition comparisons are presented. EAF inputs for the first two batches and bath temperature validation have already been presented in our previous work;<sup>[7]</sup> therefore, Table 2 and the subsequent figures only show the inputs and the results for the third and the fourth batch.

Figure 3 and 4 show the main inputs to the EAF, such as carbon injection, oxygen lancing and electric power as well

Type		Scrap	Fat coke	Lime	Dolomite	Dust	Lime	Lime	Dolomite
	Injection time [s]	0	0	0	0	0	572	634	680
	Mass [kg]	44 582	919	1040	1040	647	500	500	470
Type		Dolomite	Dolomite	Lime	Lime	Scrap	Dolomite	Lime	Scrap
Third Batch	Injection time [s]	732	772	864	911	940	1378	1438	1650
	Mass [kg]	500	460	520	510	37 068	470	510	23 788
Type		Al	SiMn	FeSi					
	Injection time [s]	3148	3148	3148					
	Mass [kg]	135	1116	153					
Type		Scrap	Fat coke	Lime	Dolomite	Dust	Brick	Dolomite	Lime
Fourth Batch	Injection time [s]	0	0	0	0	0	270	799	900
	Mass [kg]	47 294	621	1050	1020	1332	1000	500	510
Type		Dolomite	Scrap	Lime	Lime	Dolomite	Lime	Lime	Scrap
	Injection time [s]	955	1000	1007	1059	1383	1443	1493	1750
	Mass [kg]	520	37 299	500	510	500	530	520	23 907

**Table 2.** Discrete inputs to the EAF.

as comparison between the measured and the simulated bath temperatures for the third and the fourth batch.

The results are further summarized in **Table 3** showing the comparison between the measured and the simulated values of bath temperature, endpoint steel composition, and endpoint slag composition. The results of the new, enhanced model are compared to the results of our previous work<sup>[5,6]</sup> as well.

Comparison of the steel temperatures as shown in **Table 3**, panel a) shows good matching between the measured and the estimated data. The second sampling point of the second batch at 2990 s shows greater difference between both values, which is most likely a consequence of several factors. First, the investigated EAF is not equipped with any stirrers, which can lead to nonhomogeneous bath conditions and different temperature gradients throughout the bath. Hence, the molten zone temperature in an EAF is not uniform and there is a temperature gradient in the range of 80–120 K in the worst case.<sup>[30]</sup> Second, the sampling point might be near to boundary surface between the slag and steel. Third, observing the measured temperature, it increases from 1887 K at 2819 s to 1952 K at 2990 s, presenting the difference that cannot be achieved considering the total energy input to the EAF in this period. Third batch is similar to the first two. According to the FeO content in the slag, it is clear that the fourth batch does not contain foamy slag, as its content is higher than acceptable to have a

foamy slag.<sup>[31]</sup> Since equations implemented in the model consider a presence of foamy slag, the lack of the later results in simulated bath temperatures being higher than measured, as seen in **Figure 4**. Although the EAF is powered off after 3287 s of the operation, meaning that no energy has been added to the bath, the temperature at the third sampling point (3402 s) is higher than at the second sampling point (3297 s), which can again be a consequence of sampling point selection.

**Table 3**, panel b) shows the comparison between the measured and the simulated steel compositions. It can be seen that simulated fractions of dissolved elements during both samplings are very close to the measured data. A slightly larger difference in carbon content can be observed at the second sampling of the second batch, which is most likely a consequence of a nonhomogeneous bath conditions, i.e., just before sample of the bath was taken, carbon injection was engaged, with especially noticeable amount the second time. Since sampling was performed shortly after the carbon injection, insufficient time was provided for the carbon to mix uniformly throughout the bath. For this reason, the measured data are lower than the predicted data.

Furthermore, the evaluation of the model through endpoint steel compositions may not be the most appropriate validation method, since endpoint errors can occur, due to relatively small deviations in initial conditions or inputs. Better way of validating the model is

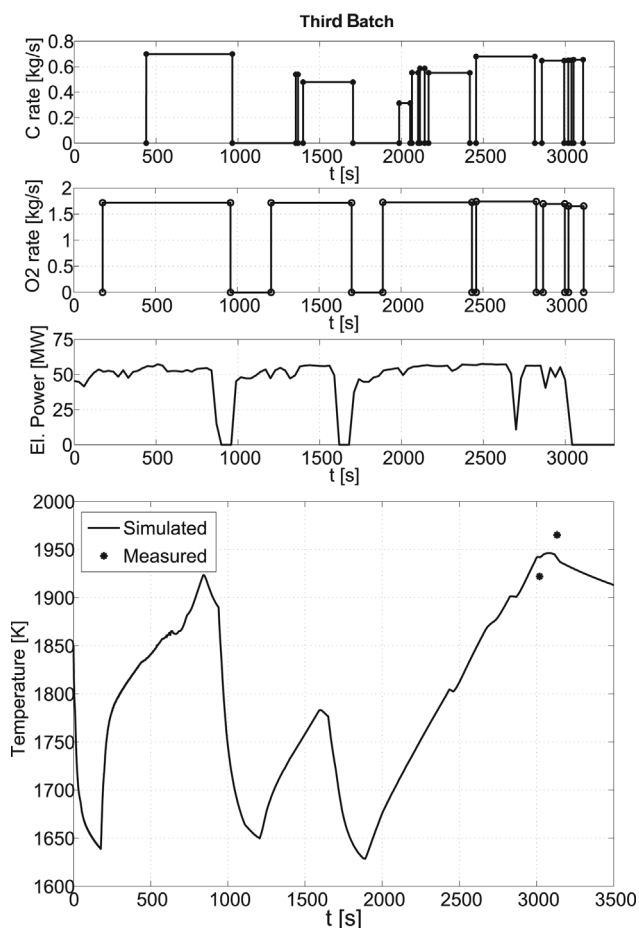


**Figure 3.** Inputs to the EAF and comparison of measured and simulated temperature for third batch.

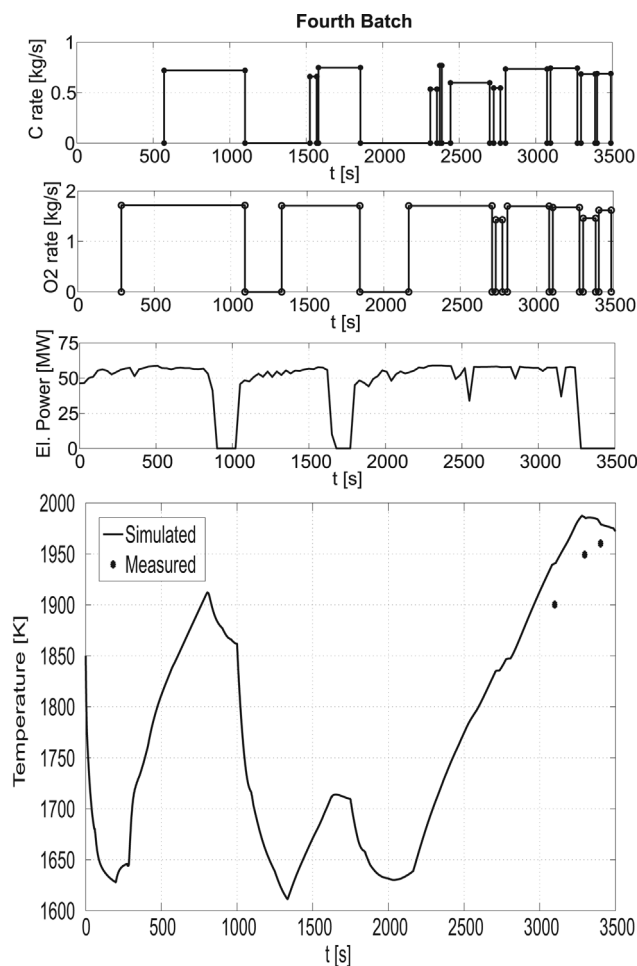


**Figure 4.** Inputs to the EAF and comparison of measured and simulated temperature for fourth batch.

through absolute errors; thus, if the second carbon measurement of second batch is neglected, the maximum error in carbon composition is 0.096%.

As can be seen in Table 3, panel c), the slag composition is estimated to  $\pm 8.5\%$  precision (except  $\text{Al}_2\text{O}_3$ ), which can be considered as a very good result. The largest errors between the measured and the simulated slag composition belong to  $\text{Al}_2\text{O}_3$  and  $\text{SiO}_2$ , where simulated percentage is lower than measured as the model does not include  $\text{Al}_2\text{O}_3$  and  $\text{SiO}_2$  change due to refractory erosion (for  $\text{Al}_2\text{O}_3$ ) and lacks accurate information about their percentage in additive materials. In the fourth case, the measured amount of  $\text{FeO}$  is higher than the expected value, which is probably caused due to the sampling point selection.

The results show acceptable differences between the measured and the predicted data. The error factors, which contribute to the deviations the most, arise from the modeling assumptions and simplifications. The most significant error factors are following. The modeled EAF is not equipped with stirring. All equations described in the present paper are based on the assumption of uniform temperature and bath distribution. Compositions of

additives and scrap baskets are not completely accurate. The model neglects certain stochastic phenomena which are otherwise present and finally, several simplifications and assumptions were made when modeling the chemical reactions.

As can be seen in Figure 4 and Table 3, the enhanced model estimates the variables of an EAF process with greater accuracy in comparison to the model presented in our previous work.<sup>[5,6]</sup> The model as presented in ref.[5,6] was validated using average values of the process measurements and not measurements for each separate charge. In this manner, the enhanced model presented here exhibits greater accuracy and greater potential for model-based control applications. Nonetheless, as mentioned previously, it has to be clear whether certain deviations that occur between simulated and measured temperatures actually originate from non-uniform bath conditions and sampling point selections or due to inaccurate model. In order to overcome the concern of an inaccurate model, energy and mass balances are calculated for each batch. The calculations revealed that

**a) Comparison between measured and simulated bath temperatures.**

	First batch		Second batch		Third batch		Fourth batch		
Time [s]	2752	2974	2819	2990	3020	3133	3099	3297	3402
Measured [K]	1902	1977	1887	1952	1922	1965	1900	1949	1960
Simulated [K]	1908	1963	1889	1925	1942	1941	1940	1986	1980

**b) Comparison between measured and simulated steel compositions**

		Time [s]	C [%]	Si [%]	Mn [%]	Cr [%]
First Batch	Measured	3207	0.057	0.012	0.229	0.008
	Old model <sup>[5,6]</sup>		0.2449	0.00687	0.2556	0.02683
	New model		0.05602	0.01148	0.2123	0.0085
Second Batch	Measured	2479	0.063	0.01	0.060	0.007
	Old model <sup>[5,6]</sup>		0.1610	0.0099	0.1479	0.0464
	New model		0.059	0.011	0.062	0.0064
Third Batch	Measured	3260	0.0620	0.212	0.522	0.009
	Old model <sup>[5,6]</sup>		0.2293	0.1952	0.5916	0.0384
	New model		0.1400	0.235	0.618	0.0086
Fourth Batch	Measured	2735	0.074	0.008	0.058	0.008
	Old model <sup>[5,6]</sup>	2512	0.2084	0.0004	0.0664%	0.0076%
	New model		0.0683	0.00692	0.0594%	0.0095%
Fourth Batch	Measured		0.092	0.011	0.08%	0.006%
	Old model <sup>[5,6]</sup>		0.1730	0.0065	0.165%	0.1278%
	New model		0.0946	0.0111	0.0749%	0.00526%

**c) Comparison between measured and simulated slag compositions.**

		Al <sub>2</sub> O <sub>3</sub> [%]	CaO+MgO+Ash [%]	Cr <sub>2</sub> O <sub>3</sub> [%]	FeO [%]	MnO [%]	SiO <sub>2</sub> [%]
First Batch	Measured	6.92	44.15	3.14	29.74	5.66	9.87
	Old model <sup>[5,6]</sup>	3.1747	36.537	1.966	47.56	3.733	7.03
	New model	4.15	47.79	2.95	30.59	5.43	9.07
Second Batch	Measured	6.77	38.62	2.120	39.44	3.34	9.32
	Old model <sup>[5,6]</sup>	3.513	35.833	1.506	48.995	2.190	7.962
	New model	4.087	41.909	2.094	39.721	3.338	8.851
Third Batch	Measured	7.04	51.49	1.64	26.53	2.98	10.32
	Old model <sup>[5,6]</sup>	2.80	49.40	1.57	34.32	2.74	9.17
	New model	3.11%	54.87	1.62	27.59	2.97	9.84
Fourth Batch	Measured	5.15	33.962	2.6%	49.63%	3.23%	6.12%
	Old model <sup>[5,6]</sup>	2.416	39.573	1.419%	47.950%	2.321%	6.321%
	New model	2.505	41.106	2.706%	44.074%	3.179%	6.430%

**Table 3.** Comparison between measured and simulated process values.

energy and mass balances obtained by the model are compatible with other similar studies and more important, measured operational data. Moreover, since matching between measured and simulated steel and slag compositions is satisfactory it can be concluded that calculation of the EAF mass balance is proper. The later almost completely determines the chemical energies, and since all other energy sources and sinks are measurable, the calculation of the overall energy balance can be considered as correct. Furthermore, simulation results for other batches, which are not shown here, have revealed that the model has sufficient accuracy. Nevertheless, deviations between simulated and actual steel compositions can occur immediately after the injection of additives, since the model assumes uniform bath conditions. These differences disappear after the bath reaches sufficient level of homogeneity. To compare the operation of the

studied EAF and other modern EAFs,<sup>[32]</sup> energy and mass balances have been calculated and are shown in **Table 4** and **Figure 5**.

Although Table 4 reveals a lower material consumption for the case study in comparison to the modern EAF, the performance evaluation of two furnaces requires establishing energy balance. Figure 5 envisages energy balance based on the four heats of the studied EAF along with the energy balance of the modern EAF<sup>[32]</sup> and a typical range of energy distribution.<sup>[33]</sup> Literature review on energy balance founded on EAFs,<sup>[33–40]</sup> shows a wide spread in the energies transferred to the sinks (off-gas in the range from 21 to 317 KWh  $t_{sc}^{-1}$ ,<sup>[33]</sup> slag in the range from 26 to 118 KWh  $t_{sc}^{-1}$ <sup>[33]</sup> and water-cooled panels in the range from 37.8 to 306 KWh  $t_{sc}^{-1}$ <sup>[33,34]</sup>). However, these variations are acceptable.<sup>[11,33]</sup> The deviations mostly originate from differences and assumptions of the models which are

Input	Studied EAF		Modern EAF <sup>[32]</sup>		Output	
	Kg of consumption per 1 ton of steel		Kg of production per 1 ton of steel		Stuited EAF	
Ferrous materials					Molten	1000
Scrap	973.2		N.A <sup>a)</sup>		Slag	89.3
Hot heel <sup>b)</sup>	109.5		N.A		Offgas	140.2
Gas						
Oxygen lanced	37.3		67.2			
Natural gas	0		7.1			
Air infiltrated	71.5		N.A			
Additives						
Carbon injected	10.0		7.9			
Carbon charged	7.6		16.8			
Lime	29.1		N.A			
Dolime	23.2		N.A			
Brick	2.4 <sup>c)</sup>		N.A			
Dust	8 <sup>c)</sup>		N.A			
FeMn	1.56 <sup>d)</sup>		N.A			
FeSi	1.62 <sup>d)</sup>		N.A			
SiMn	10.8 <sup>d)</sup>		N.A			
Al	1.23 <sup>d)</sup>		N.A			

a) N.A: Not Available; b) Hot heel mass is divided by the first basket mass; c) Brick and dust are not injected in all heats; d) In case that it is injected.

**Table 4.** Mass balance of the studied EAF in comparison with a modern EAF.<sup>32</sup>

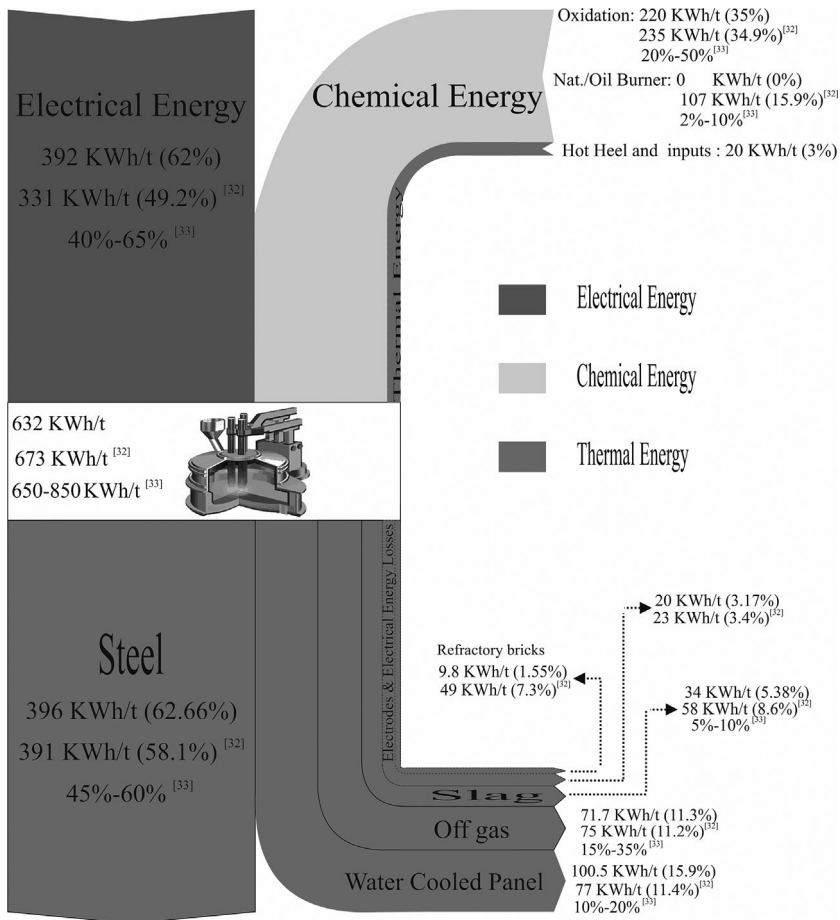


**Figure 5.** Energy balance based on four heats of the studied EAF in comparison with a modern EAF<sup>[32]</sup> in a typical range of energy distribution.<sup>[33]</sup>

used to predict the energy balance, EAF structure and installed equipment, input regime, quality of input materials, and initial operational conditions.

As seen in Figure 5, energy losses in electrodes and secondary electrical circuits are for both EAFs on the same level; however, there is a noticeable difference among the estimation of the energy transferred to slag, off-gas, and water-cooled panels. Nonetheless, the estimations are in the satisfactory margins. The slag enthalpy computed for the case study is similar to the results addressed in ref.<sup>[37-40]</sup>

## 4. Conclusion

In the paper, a comprehensive EAF model is presented, intended for simulation purposes and development of the model-based control systems of an EAF. It approximates all the significant phenomena and dynamic conditions in the EAF with sufficient accuracy. In comparison to other existing models, an arc module has been added, which predicts the energy dissipation and is useful when

determining the suitable arc length and arc current (transformer tap). Moreover, thermal module describes all possible states emerging during the melting due to changes in arc length, slag height and bath height. Furthermore, in comparison to the chemical-slag module presented in our previous work,<sup>[5,6]</sup> the coefficients denoting the fraction of each component to react with oxygen have been modified and equations have been revised accordingly. As it has been shown in the results, the modified coefficients lead to more accurate estimation results. Since the equations used in the model are based on fundamental laws of physics, the model can be used to simulate any EAF.

As the model validation shows, the results are comparable with the measured data, which indicates an improvement in accuracy and versatility of the designed EAF model. Whether the studied EAF was equipped with an appropriate stirring, the accuracy of the model should have been even higher, as it assumes homogeneity in each zone. Since calculation times and model accuracy are satisfactory, the model can be employed to monitor EAF processes and/or to establish EAF energy and mass balance to evaluate operation and energy saving

Zone	States	Rate of energy change
sSc	A-G	$Q_{sSc\xi} = Q_{Conv sSc-\xi} + Q_{CH_4-sSc\xi} - Q_{Conv sSc-\xi} \text{ a)}$
ISc	A-G	$Q_{ISc} = Q_{arc-ISc} + Q_{chem-ISc} + Q_{CH_4-ISc} - [Q_{Conv ISc-ISI} + Q_{Conv ISc-wall} + Q_{Conv ISc-floor} + \sum_{\xi=1}^N Q_{Conv ISc-s\xi} + Q_{ISc-HBI}]$ ,
SI	A-G	$Q_{SI} = Q_{Conv SI-SI}$
ISI	G	$Q_{ISI} = Q_{arc-ISI} + Q_{Conv ISc-ISI} + Q_{chem-ISI} + Q_{CO Post-ISI} - [ \sum_{p=1}^M Q_{Conv ISI-sI} + Q_{Conv ISI-gas} + Q_{Conv ISI-wall} + Q_{Conv ISI-water} + Q_{Rad ISI-electrode} + Q_{Rad ISI-roof} ]$ ,
A, D		$Q_{ SI} = Q_{arc-ISI} + Q_{Conv ISc-ISI} + Q_{chem-ISI} + Q_{CO Post-ISI} - [ \sum_{p=1}^M Q_{Conv ISI-sI} + Q_{Conv ISI-gas} + Q_{Conv ISI-wall} + Q_{Conv ISI-water} + Q_{Rad ISI-electrode} + Q_{Rad ISI-roof} ]$ ,
F		$Q_{ SI} = Q_{arc-ISI} + Q_{Conv ISc-ISI} + Q_{chem-ISI} + Q_{CO Post-ISI} - [ \sum_{p=1}^M Q_{Conv ISI-sI} + Q_{Conv ISI-gas} + Q_{Conv ISI-wall} + Q_{Rad ISI-water} + Q_{Conv ISI-electrode} + Q_{Rad ISI-roof} + Q_{Rad ISI-wall} ]$ ,
B, C, E		$Q_{ SI} = Q_{arc-ISI} + Q_{Conv ISc-ISI} + Q_{chem-ISI} + Q_{CO Post-ISI} - [ \sum_{p=1}^M Q_{Conv ISI-sI} + Q_{Conv ISI-gas} + Q_{Conv ISI-wall} + Q_{Rad ISI-water} + Q_{Rad ISI-electrode} + Q_{Rad ISI-roof} + Q_{Rad ISI-wall} ]$ ,
Gas	B, E	$Q_{gas} = Q_{Conv arc-gas} + Q_{CO Post-gas} + Q_{Conv ISc-gas} \text{ or } Q_{Conv sSc1-gas} * + Q_{CH_4-gas} - [ Q_{conv gas-roof} + Q_{Conv gas-water} + Q_{Conv gas-wall} + Q_{O_2-Stream Injection} + Q_{O_2-Stream Injection} + Q_{O_2-Post} + Q_{off gas} + Q_{leak air} + Q_{hatch} ]$ ,
C, F		$Q_{gas} = Q_{CO Post-gas} + Q_{Conv ISc-gas} + Q_{CH_4-gas} - [ Q_{Conv gas-roof} + Q_{Conv gas-water} + Q_{Conv gas-wall} + Q_{Conv gas-electrode} + Q_{O_2-Stream Injection} + Q_{O_2-Post} + Q_{off gas} + Q_{leak air} + Q_{hatch} ]$ ,
A		$Q_{gas} = Q_{Conv arc-gas} + Q_{CO Post-gas} + Q_{Conv ISc-gas} \text{ or } Q_{Conv sSc1-gas} * + Q_{CH_4-gas} - [ Q_{Conv gas-roof} + Q_{Conv gas-water} + Q_{Conv gas-electrode} + Q_{O_2-Stream Injection} + Q_{O_2-Post} + Q_{off gas} + Q_{leak air} + Q_{hatch} ]$ ,

Table 5. Continued

Zone	States	Rate of energy change
	D, G	$Q_{\text{gas}} = Q_{\text{CO Post-gas}} + Q_{\text{ConvISI-gas}} + Q_{\text{CH}_4\text{-gas}} + Q_{\text{ConvGas-roof}} + Q_{\text{ConvGas-water}} + Q_{\text{ConvGas-electrode}} + Q_{\text{O}_2\text{-Stream Injection}} + Q_{\text{O}_2\text{-Post}} + Q_{\text{Off-gas}} + Q_{\text{leak air}} + Q_{\text{hatch}}$ ;
Electrode	F	$Q_{\text{electrode}} = Q_{\text{Ohmic}} + Q_{\text{arc-electrode}} + Q_{\text{ConvGas-electrode}} + Q_{\text{ConvISI-electrode}} - [Q_{\text{RadElectrode-ISI}} + Q_{\text{RadElectrode-water}} + Q_{\text{RadElectrode-wall}} + Q_{\text{RadElectrode-roof}}]$ ;
	B, C	$Q_{\text{electrode}} = Q_{\text{Ohmic}} + Q_{\text{arc-electrode}} + Q_{\text{ConvGas-electrode}} - [Q_{\text{RadElectrode-ISI}} + Q_{\text{RadElectrode-water}} + Q_{\text{RadElectrode-wall}} + Q_{\text{RadElectrode-roof}}]$ ;
	G	$Q_{\text{electrode}} = Q_{\text{Ohmic}} + Q_{\text{arc-electrode}} + Q_{\text{ConvGas-electrode}} + Q_{\text{ConvISI-electrode}} - [Q_{\text{RadElectrode-ISI}} + Q_{\text{RadElectrode-water}} + Q_{\text{RadElectrode-roof}}]$ .
	A, D, E	$Q_{\text{electrode}} = Q_{\text{Ohmic}} + Q_{\text{arc-electrode}} + Q_{\text{ConvGas-electrode}} - [Q_{\text{RadElectrode-ISI}} + Q_{\text{RadElectrode-water}} + Q_{\text{RadElectrode-roof}}]$ .
Water	A	$Q_{\text{water}} = Q_{\text{Radarc-water}} + Q_{\text{ConvISI-water}} + Q_{\text{Rad}} + Q_{\text{RadElectrode-water}} + Q_{\text{ConvGas-water}} - Q_{\text{Radwater-roof}}$ ;
	E	$Q_{\text{water}} = Q_{\text{Radarc-water}} + Q_{\text{Rad}} + Q_{\text{RadElectrode-water}} + Q_{\text{ConvGas-water}} - Q_{\text{Radwater-roof}}$ ;
	D, G	$Q_{\text{water}} = Q_{\text{RadISI-water}} + Q_{\text{ConvISI-water}} + Q_{\text{RadElectrode-water}} + Q_{\text{ConvGas-water}} - Q_{\text{Radwater-roof}}$ .
	B, C, F	$Q_{\text{water}} = Q_{\text{Radwall-water}} + Q_{\text{RadElectrode-water}} + Q_{\text{RadISI-water}} + Q_{\text{ConvGas-water}} - Q_{\text{Radwater-roof}}$ .
Wall	B, E	$Q_{\text{wall}} = Q_{\text{Radarc-wall}} + Q_{\text{ConvISI-wall}} + Q_{\text{ConvGas-wall}} + Q_{\text{RadISI-wall}} - [Q_{\text{Radwall-water}} + Q_{\text{Radwall-roof}}]$ ;
	C, F	$Q_{\text{wall}} = Q_{\text{ConvISC-wall}} + Q_{\text{ConvISI-wall}} + Q_{\text{ConvGas-wall}} + Q_{\text{RadISI-wall}} - [Q_{\text{Radwall-water}} + Q_{\text{Radwall-roof}}]$ ;
	A, D, G	$Q_{\text{wall}} = Q_{\text{ConvISC-wall}} + Q_{\text{ConvISI-wall}}$
	B, C, E, F	$Q_{\text{roof}} = Q_{\text{ConvGas-roof}} + Q_{\text{RadISI-roof}} + Q_{\text{RadElectrode-roof}} + Q_{\text{Radwall-roof}} + Q_{\text{Radwater-roof}}$
Floor	A, D, G	$Q_{\text{roof}} = Q_{\text{ConvGas-roof}} + Q_{\text{RadISI-roof}} + Q_{\text{RadElectrode-roof}} + Q_{\text{Radwater-roof}}$ ;
	A-G	$Q_{\text{floor}} = Q_{\text{ConvISC-floor}}$

a) Before slag formation.

**Table 5.** Energy balance equations for EAF zones.

potentials. Furthermore, capability of predicting the slag height and arc energy dissipation promote the model as a model-based control system in order to determine the appropriate strategy of EAF inputs to either reduce energy consumption, achieve better steel quality or yield.

### Acknowledgements

The paper received funding from Sharif Research Energy Institute (SERI), project *Simulation and control of an EAF*. The support of SERI is kindly acknowledged.

### Appendix

**Table 5:** the list of equations needed to compute the EAF energy balance for each zone in accordance to Table 1.

Received: March 9, 2016; Revised: May 25, 2016

**Keywords:** chemical model; EAF; experimental validation; heat transfer model; modeling; reference energy system

### References

- [1] *World Steel in Figures 2012*, World steel association, Belgium 2012.
- [2] R. J. Fruehan, O. Fortini, H.W. Paxton, R. Brindle, *Theoretical Minimum Energies to Produce Steel for Selected Conditions*, U.S. Department of Energy, Washington, USA 2000.
- [3] J. G. Bekker, I. K. Craig, P. C. Pistorius, *ISIJ Int.* 1999, 39, 23.
- [4] R. D. M. MacRosty, C. L. E. Swartz, *Ind. Eng. Chem. Res.* 2005, 44, 8067.
- [5] V. Logar, D. Dovzan, I. Škrjanc, *ISIJ Int.* 2012, 52, 402.
- [6] V. Logar, D. Dovzan, I. Škrjanc, *ISIJ Int.* 2012, 52, 413.
- [7] A. H. Fathi, Y. Saboohi, I. Škrjanc, V. Logar, *ISIJ Int.* 2015, 55, 1353.
- [8] D. J. Oosthuizen, J. H. Viljoen, I. K. Craig, P. C. Pistorius, *ISIJ Int.* 2001, 41, 399.
- [9] D. Potey, B. Bowman, S. Alameddine, *8th EEC*, IOM Communications, Birmingham, UK 2005.
- [10] M. M. Rahman, *PhD thesis*, University of New South Wales 2010.
- [11] J. A. Jones, B. Bowman, P. A. Lefrank, *The Making, Shaping and Treating of Steel*, The AISE Steel Foundation, Pittsburgh, USA 1998, Ch. 10.
- [12] E. B. Pretorius, R. C. Carlisle, *56th EAF Conference*, Iron and Steel Society, New Orleans, USA 1998.
- [13] S. Aminorroaya, H. Edris, *7th EEC*, AIM, Venice, Italy 2002.
- [14] D. Lotun, L. Pilon, *ISIJ Int.* 2005, 45, 835.
- [15] L. P. Rathaba, *Master thesis*, University of Pretoria, Pretoria, South Africa 2004.
- [16] N. Arzpeyma, *Master thesis*, Royal Institute of Technology, Stockholm, Sweden 2011.
- [17] F. Memoli, M. Guzzon, C. Giavani, *AISTech*, Indianapolis, USA 2011.
- [18] J. L. G. Sanchez, M. A. Ramirez-Argaez, A. N. Conejo, *Steel Res. Int.* 2009, 80, 113.
- [19] V. Logar, I. Škrjanc, *ISIJ Int.* 2012, 52, 1225.
- [20] M. Kaviany, *Essentials of Heat Transfer: Principles, Materials, and Applications*, Cambridge University Press, New York, USA 2011, 350.
- [21] V. Logar, A. H. Fathi, I. Škrjanc, *Steel Res. Int.* 2015, 87, 330.
- [22] N. Arzpeyma, O. Widlund, M. Ersson, P. Jönsson, *ISIJ Int.* 2013, 53, 48.
- [23] F. Kreith, R. F. Boehm, G. D. Raithby, K. G. T. Hollands, N. V. Suryanarayana, M. F. Modest, V. P. Carey, J. C. Chen, N. Lior, R. K. Shah, K. J. Bell, R. J. Moffat, A. F. Mills, A. E. Bergles, L. W. Swanson, V. W. Antonetti, T. F. Irvine, M. Capobianchi, *Heat and Mass Transfer Mechanical Engineering Handbook*, CRC Press LLC, Boca Raton, USA 1999.
- [24] G. Bisio, G. Rubatto, R. Martini, *Energy* 2000, 25, 1047.
- [25] Y. Jaluria, *Natural Convection: Heat and Mass Transfer*, Vol. 5, Pergamon Press, Oxford, UK 1980.
- [26] F. Qian, B., Farouk, R. Mutharasan, *Metall. Mater. Trans. B* 1995, 26, 1057.
- [27] R. R. Ahmad, N. Yaacob, A. H. Mohd Murid, *Int J. Comput. Math.* 2004, 81, 1407.
- [28] R. L. Burden, J. D. Faires, *Numerical Analysis*, Cengage Learning, Boston, USA 2010, Ch. 5.
- [29] B. E. Poling, G. H. Thomson, D. G. Friend, R. L. Rowley, W. V. Wilding, *Perry's Chemical Engineers Handbook*, Vol. 2, McGraw-Hill, New York, USA 2008.
- [30] O. J. P. Gonzalez, M. A. Ramirez-Argaez, A. N. Conejo, *ISIJ Int.* 2010, 50, 1.
- [31] A. Opfermann, D. Riedinger, 9th EEC, Krakow, Poland 2008.
- [32] Y. N. Toulouevski, I. Y. Zinurov, *Innovation in Electric Arc Furnaces*, Springer-Verlag Berlin Heidelberg, Berlin, Germany 2010.
- [33] M. Kirschen, V. Risonarta, H. Pfeifer, *Energy* 2009, 34, 1065.
- [34] B. Lee, I. Sohn, *JOM*, 2014, 66, 1581.
- [35] U. Camdali, M. Tunç, *Appl. Therm. Eng.* 2003, 23, 2255.
- [36] M. Barati, S. Esfahani, T. A. Utigard, *Energy* 2011, 36, 5440.
- [37] E. Evenson, H. Goodfellow, M. Kempe, *58th EAF Conference*, Iron and Steel Society, Orlando, USA 2000.
- [38] M. Kirschen, H. Pfeifer, F. Wahlers, *7th EEC*, AIM, Venice, Italy 2002.
- [39] J. Jones, *60th EAF Conference*, Iron and Steel Society, San Antonio, USA 2002.
- [40] M. Kendall, M. Thys, A. Horrex, J. Verhoeven, *9th EEC*, SITPH, Krakow, Poland 2008.